Modeling Condensation in Deep Convection

WOJCIECH W. GRABOWSKI

Mesoscale and Microscale Meteorology Laboratory, National Center for Atmospheric Research,[a] Boulder, Colorado, and Institute of Geophysics, Faculty of Physics, University of Warsaw, Warsaw, Poland

HUGH MORRISON

Mesoscale and Microscale Meteorology Laboratory, National Center for Atmospheric Research,[a] Boulder, Colorado

(Manuscript received 1 September 2016, in final form 18 April 2017)

ABSTRACT

Cloud-scale models apply two drastically different methods to represent condensation of water vapor to form and grow cloud droplets. Maintenance of water saturation inside liquid clouds is assumed in the computationally efficient saturation adjustment approach used in most bulk microphysics schemes. When super- or subsaturations are allowed, condensation/evaporation can be calculated using the predicted saturation ratio and (either predicted or prescribed) mean droplet radius and concentration. The study investigates differences between simulations of deep unorganized convection applying a saturation adjustment condensation scheme (SADJ) and a scheme with supersaturation prediction (SPRE). A double-moment microphysics scheme with CCN activation parameterized as a function of the local vertical velocity is applied to compare cloud fields simulated applying SPRE and SADJ. Clean CCN conditions are assumed to demonstrate upper limits of the SPRE and SADJ difference. Microphysical piggybacking is used to extract the impacts with confidence. Results show a significant impact on deep convection dynamics, with SADJ featuring more cloud buoyancy and thus stronger updrafts. This leads to around a 3% increase of the surface rain accumulation in SADJ. Upper-tropospheric anvil cloud fractions are much larger in SPRE than in SADJ because of the higher ice concentrations and thus longer residence times of anvil particles in SPRE, as demonstrated by sensitivity tests. Higher ice concentrations in SPRE come from significantly larger ice supersaturations in strong convective updrafts that feature water supersaturations of several percent.

1. Introduction

Condensation of water vapor to form and grow cloud droplets is one of the most fundamental processes of cloud and precipitation formation. It drives cloud-scale dynamics through the release of latent heat and determines the strength of convective updrafts. Cloud-scale models simulate condensation by applying two drastically different methods [see, for instance, Grabowski and Jarecka (2015, hereinafter GJ15) and references therein]. The first is the bulk condensation where water-saturated conditions are assumed inside liquid clouds. Bulk condensation is calculated by assuming that all water vapor in excess of saturation is converted into cloud water, maintaining saturated conditions at the completion of the model time step. Conversely, bulk evaporation is calculated by evaporating enough water to maintain saturated conditions at the end of the time step. Saturation adjustment is computationally efficient because it typically does not constrain the model time step and allows straightforward implementation of the centered-in-time differencing (e.g., Grabowski and Smolarkiewicz 2002). Most bulk cloud microphysics schemes apply saturation adjustment to model condensation (e.g., Lin et al. 1983; Rutledge and Hobbs 1984; Ferrier 1994; Grabowski 1998, 1999; Hong et al. 2004; Thompson et al. 2004; Milbrandt and Yau 2005; Morrison et al. 2009).

The second approach involves prediction of the in-cloud super- or subsaturation and calculation of the condensation/evaporation based on the predicted saturation ratio. Such an approach is typically used in microphysical schemes that predict not only condensate

---

[a] The National Center for Atmospheric Research is sponsored by the National Science Foundation.

Corresponding author: Wojciech W. Grabowski, grabow@ucar.edu

DOI: 10.1175/JAS-D-16-0255.1

mass but also relevant features of the droplet size distribution (e.g., the droplet concentration and mean radius), such as double-moment bulk or bin microphysics schemes [e.g., Cotton et al. (2003), Phillips et al. (2007), and Mansell et al. (2010) for bulk schemes; Kogan (1991), Khain et al. (2004), and Lebo and Seinfeld (2011) for bin schemes]. However, many double-moment schemes still use saturation adjustment (e.g., Ferrier 1994; Cohard and Pinty 2000; Milbrandt and Yau 2005; Morrison et al. 2009). Predicting in-cloud super- or subsaturation is numerically cumbersome and often requires short time steps for numerical stability. The quasi-analytic approach for the supersaturation evolution (Clark 1973; Morrison and Grabowski 2008a) mitigates some of these problems. Moreover, the supersaturation field near cloud edges typically features large fluctuations (e.g., Grabowski 1989; Stevens et al. 1996) that can significantly affect droplet activation. These can only be avoided through a properly designed numerical procedure in which evolution of the temperature and moisture is controlled by an independently evolving supersaturation field, as in Clark (1973) [see Grabowski and Morrison (2008) for details]. More importantly, since ice initiation in deep convection is tied to the cloud water and drizzle/rain transported from the lower troposphere in convective updrafts, details of the condensational growth can also have a significant impact on the ice field development. This will be one of the key points documented in the current study.

GJ15 discuss these two approaches to modeling condensation for the case of shallow nonprecipitating convection. They show that a bulk scheme with saturation adjustment provides more buoyancy than a bin scheme with explicit super-/subsaturation prediction because of greater latent heating, but the impact on shallow convective updrafts is relatively minor. This is because supersaturations are typically small (i.e., below 1%) for shallow convection updrafts, given their fairly weak vertical velocities. The 1% supersaturation gives about a 0.1-K reduction of the potential density (buoyancy) temperature between the two approaches to condensation for temperatures and pressures typical for warm shallow convection [see section 2, (6), and Fig. 1 in GJ15]. This small impact on the updraft dynamics in shallow convection agrees with results discussed in Clark (1973). GJ15 also show that the saturation adjustment applied for the bulk evaporation of cloud water near cloud edges results in a significant reduction of the cloud fraction when compared to the bin scheme.

The validity of the saturation adjustment approach for simulating moist convection has been questioned in the past (see discussion relevant to shallow convection in GJ15). As far as deep convection is concerned, Lebo et al. (2012, Fig. 13 therein) show large supersaturations in the case of supercell simulations. Because supercells feature strong vertical velocities (up to several tens of meters per second), large supersaturations should not be surprising. As Grabowski and Morrison (2016, hereinafter GM16) document, large supersaturation can also exist within simulations of unorganized (scattered) deep convection, like that over the Amazon basin.

GJ15 applied microphysical piggybacking (Grabowski 2014, 2015) to document the impact of saturation adjustment with high fidelity. The main idea behind the piggybacking method is to apply two sets of thermodynamic variables (the potential temperature, water vapor mixing ratio, and all variables describing aerosol, cloud, and precipitation particles) in a single cloud field simulation. The first set is coupled to the dynamics and drives the simulation (D set), and the second set piggybacks the simulated flow but does not affect it (P set). Because the two sets are driven by the same flow, the methodology allows assessing the microphysical impact with high accuracy, and it is capable of detecting even minuscule impacts on bulk cloud properties, such as the cloud cover, liquid and ice water path, and surface precipitation (Grabowski 2014). It also allows for comparing local cloud buoyancies between driving and piggybacking sets of thermodynamic variables and thus exploring possible impacts on cloud dynamics. The impact on the dynamics is assessed by performing a second simulation with the microphysical sets swapped so the D set becomes the P set, and vice versa. Although the second simulation features a different flow realization, the comparison of the two simulations allows for assessing the impact of cloud microphysics on the cloud dynamics. In a nutshell, if the difference between results from the D and P sets in the two simulations (i.e., in the original simulation and in the one with sets swapped) are the same except for the sign, then the cloud dynamics is arguably insignificantly affected by the cloud microphysics. Grabowski (2014, 2015) documented the fidelity of the piggybacking methodology in simulations of shallow and deep convection, respectively. Unequivocal separation of the microphysical and dynamical impacts on moist convection by swapping the D and P sets is the key advantage of the piggybacking methodology over the kinematic (prescribed flow) strategy used in the past to compare simulations with various microphysical schemes (e.g., Szumowski et al. 1998; Morrison and Grabowski 2007; Shipway and Hill 2012).

GM16 discuss piggybacking simulations applying a double-moment microphysics scheme with the explicit prediction of the supersaturation field to investigate the impact of pollution aerosols on deep convection. The idealized setup follows the case of daytime convective development over land based on observations during the Large-Scale Biosphere–Atmosphere (LBA) field project in Amazonia as in Grabowski (2015). GM16 show that the simulated in-cloud supersaturations are large, up to several percent in both pristine and polluted conditions, and they call into question results from deep convection simulations applying microphysical schemes with saturation adjustment. The latter provides motivation for the investigation reported here. In addition, GM16 document a significant impact of assumed CCN characteristics on the upper-tropospheric convective anvils. As discussed in the current manuscript, similar differences exist between simulations applying saturation adjustment and simulations with the supersaturation prediction.

This paper follows GM16 by using the same model and double-moment microphysics scheme (with some modifications as discussed herein), the same modeling setup, and the same piggybacking methodology. These are briefly reviewed in the next section with the emphasis on modifications of the double-moment scheme to allow saturation adjustment and to include CCN activation as a function of aerosol properties and vertical velocity. Section 3 discusses piggybacking simulations and contrasts results obtained applying microphysical schemes with the supersaturation prediction and with saturation adjustment. To better understand the differences, we introduce modifications to the microphysics scheme and discuss resulting sensitivity simulations in section 4. The discussion in section 5 concludes the paper.

2. The model and modeling case

The dynamic model used in this study, the same as in Grabowski (2014, 2015), GJ15, and GM16, is a simplified serial version of the 3D nonhydrostatic anelastic Eulerian/semi-Lagrangian (EULAG) model (http://www.mmm.ucar.edu/eulag/), referred to as the baby-EULAG. The same modeling setup as in GM16 is used here with the double-moment scheme of Morrison and Grabowski (2007, 2008a,b) (see the discussion in GM16).

The double-moment microphysics scheme (Morrison and Grabowski 2007, 2008a,b) predicts mass and number mixing ratios for cloud water (q_c and N_c) and rain (q_r and N_r). For ice, the scheme predicts the number mixing ratio for ice particles N_i and two mixing ratios describing the bulk mass of ice grown by the diffusion of water vapor q_{id} and by accretion of supercooled water q_{ir}. See the discussion concerning motivations for such an approach and examples of simulations applying it in Morrison and Grabowski (2008b) and in GM16. (Note that the symbols defined here will be used in Figs. 8 and 9.)

Two versions of the microphysics scheme are used. The first applies saturation adjustment (SADJ) to calculate cloud water condensation/evaporation (CE) using

$$\mathrm{CE} = \frac{q_v - q_s}{\Delta t\left(1 + \dfrac{L_v^2 q_s}{c_p R_v T^2}\right)}, \qquad (1)$$

where q_v and q_s are the water vapor mixing ratio and the water vapor mixing ratio at saturation, L_v is the latent heat of vaporization, c_p is the specific heat of air at constant pressure, R_v is the gas constant for water vapor, T is temperature, and Δt is the model time step. In subsaturated conditions ($q_v < q_s$), (1) is limited by the amount of available cloud water. Numerically, (1) is applied following the centered-in-time approach, as discussed in section 2b of Grabowski and Smolarkiewicz (2002). This ensures that microphysical processes are calculated from a thermodynamic state that is at near–water saturation inside liquid clouds. As in most bulk schemes applying saturation adjustment, rain evaporation and ice deposition/sublimation are calculated explicitly from the saturation ratio diagnosed from the temperature and water vapor mixing ratio fields, while rain condensation is neglected.

The second version calculates cloud water condensation/evaporation explicitly [supersaturation prediction (SPRE)]. The approach is described in Morrison and Grabowski (2008a). Absolute supersaturation, equal to the water vapor mixing ratio minus the saturation mixing ratio, is a prognosed variable, with corresponding adjustments for consistency between the temperature, water vapor, and cloud water described by Grabowski and Morrison (2008) to avoid spurious oscillations of saturation ratio near cloud edges. An overview of the approach is given in the appendix, including a brief description of new improvements. It is emphasized that, other than the treatment of condensation/evaporation, SADJ and SPRE are identical. Note that throughout the paper the word "supersaturation" refers to the water supersaturation: that is, the supersaturation with respect to a planar surface of liquid water.

To allow meaningful comparison, a simple diagnostic CCN activation scheme is used for both the SADJ and SPRE simulations. This approach is based on Abdul-Razzak and Ghan (2000), and it relates the number mixing ratio of activated CCN to the local updraft speed as well as to the local temperature and pressure and aerosol composition and size distribution. This contrasts with the explicit droplet activation scheme as a function of the predicted supersaturation used in GM16, which cannot be used with SADJ since these simulations have no supersaturation by design. Here, following Morrison and Grabowski (2008a), the number mixing ratio of previously activated CCN is a model prognostic variable. At each time step and grid location, the prognostic number of previously activated CCN is compared to the number activated using the Abdul-Razzak and Ghan (2000) scheme. If the former is smaller than the latter, the difference

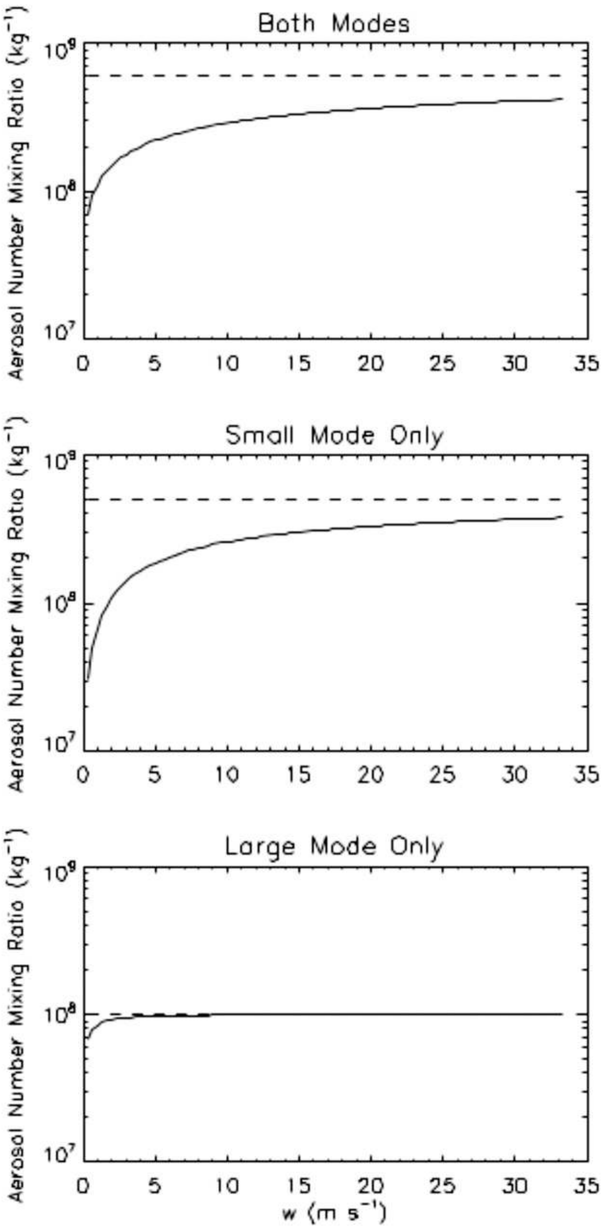

FIG. 1. Activated CCN number mixing ratio as a function of the vertical velocity as represented in the CCN activation parameterization used in this study. (top) The dependence for the two CCN modes; (middle),(bottom) dependencies when only the small or large mode is included, respectively.

represents the activation of new droplets during the time step. We use a double-mode CCN distribution as applied in pristine sensitivity ensemble simulations in GM16 (see section 4 therein). The first CCN mode is characterized by the mean dry radius of 0.05 μm and the number mixing ratio of 100 mg^{-1}. The second mode assumes mean dry radius of 0.01 μm and number mixing ratio of 500 mg^{-1}. For illustration, Fig. 1 shows the concentration of activated CCN as a function of updraft velocity for a temperature 283.15 K and a pressure of 850 hPa. We focus on pristine environmental conditions because supersaturations in clouds developing in such an environment are larger compared to polluted conditions, and the simulations provide an upper limit for the expected impact. However, simulated supersaturations inside strong updrafts of polluted clouds are still large (several percent; see Figs. 9 and 13 in GM16), and the difference between simulations applying saturation adjustment and those with the supersaturation prediction are expected to be significant for the polluted conditions as well.

Primary ice initiation is the same as GM16. Deposition/condensation-freezing nucleation is parameterized following the supersaturation-dependent formulation of Meyers et al. (1992), applied at temperatures below −8°C and ice supersaturation greater than 5%, and limited to a maximum ice concentration of 100 L^{-1}. The concentration of existing ice is compared to the concentration diagnosed from the Meyers et al. (1992) formulation, and if the concentration diagnosed from the Meyers formula is larger than the concentration of existing ice, then the difference is the concentration of new ice crystals that are nucleated. This is similar to the approach used in most microphysics schemes that do not explicitly track ice nuclei (e.g., Thompson et al. 2004; Milbrandt and Yau 2005; Morrison et al. 2009). Cloud droplet and raindrop heterogeneous freezing follows the volume-dependent formulation of Bigg (1953). Contact freezing of cloud droplets follows the approach in Morrison and Pinto (2005). Homogeneous freezing of all cloud and rainwater is assumed to occur at −40°C. Ice initiation by rime splintering is calculated following Hallett and Mossop (1974).

The modeled case simulates daytime convective development over warm-season continents and features a transition from shallow to deep convection as a result of strongly increasing surface latent and sensible heat fluxes. The 12-h simulations (i.e., from 0730 to 1930 local time) apply evolving surface fluxes as in Grabowski et al. (2006) [see Fig. 1 in Grabowski (2015) and the appendix in Grabowski et al. (2006)]. The model setup is exactly the same as in Grabowski (2015) and GM16. The horizontal domain of 50 km by 50 km is covered with a uniform 400-m grid. In the vertical, the domain extends up to 24 km, applying 81 levels with a stretched grid. The vertical grid length is around 100 m near the surface, with about a dozen levels below 1.5 km. The vertical grid length increases to about 300 and 400 m at 5 and 15 km, respectively. The model time step is 4 s.

We apply the piggybacking methodology following GM16. In the first ensemble of simulations, SPRE drives and SADJ piggybacks the predicted flow. The ensemble includes five members, with individual simulations referred

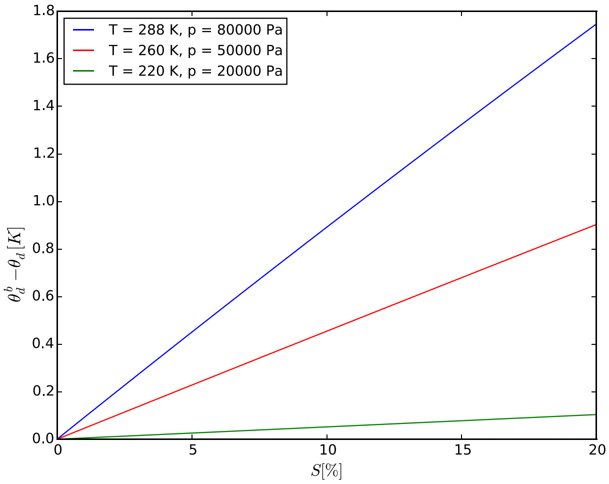

FIG. 2. Difference between potential density temperatures using saturation adjustment θ_d^b and allowing supersaturation θ_d as a function of the supersaturation S. See (6) in GJ15. Green, red, and blue lines correspond to conditions of upper, middle, and lower troposphere, respectively, with specific pressure and temperature values shown in the key.

to as D-SPRE/P-SADJ. As in GM16, ensemble members are generated by applying different sets of random numbers to the temperature, moisture, and prescribed surface fluxes. In the second five-member ensemble, SADJ drives and SPRE piggybacks the predicted flow. These simulations are referred to as D-SADJ/P-SPRE.

As in GM16, simulation results are saved as snapshots of model fields every 6 min of the simulation time, and surface precipitation rate is saved every 3 min as the average over all time steps from the preceding 3-min period. These data are used in the analysis of model results discussed in the next section.

3. Results

a. Buoyancy and updraft statistics

GJ15 provide a theoretical argument for the impact of nonzero supersaturations on the cloud buoyancy [see their section 2 and (6)] and document the impact on simulations of shallow nonprecipitating convection. Since the range of temperatures and pressures as well as the supersaturations is significantly larger in the case of deep convection, Fig. 2 shows the difference in the potential density temperature [defined as $\theta_d = \theta(1 + \varepsilon q_v - q_c - q_r - q_{id} - q_{ir})$ where $\varepsilon = R_v/R_d - 1$ and R_v and R_d are the gas constants for water vapor and dry air, respectively], calculated assuming either saturation adjustment or a finite supersaturation and derived for conditions that approximately correspond to the lower, middle, and upper troposphere. The decreasing slope of the lines represents decreasing amount of water vapor available for saturation adjustment when one moves from the lower to the upper troposphere. A 10% supersaturation gives a small increase of buoyancy in the upper troposphere when saturation adjustment is used. However, in the middle and lower troposphere, the differences are relatively large, about 0.4 and 0.8 K, respectively.

To document the link between nonzero supersaturations and in-cloud buoyancy, Fig. 3 shows statistics of the potential density temperature difference between the cloud and environmental profiles for hours 5–8. Only points with vertical velocity larger than 1 m s^{-1} and the sum of cloud water and ice mixing ratio larger than 0.1 g kg^{-1} are considered. This figure shows profiles of the median potential density temperature difference from sets D of thermodynamic variables for all ensemble members (solid lines) and the difference between the median from sets D and P (multiplied by 4 to fit the scale; dashed lines). In general, differences between median profiles for D-SPRE and D-SADJ are small. This perhaps agrees with the fact that only extreme buoyancies are significantly affected by large supersaturations (i.e., for large vertical velocities). The D minus P median profiles [dashed lines; positive (negative) for D-SADJ (D-SPRE)] are relatively small. However, the magnitude of the difference is larger when SADJ drives (top panels). This is consistent with stronger updrafts when SADJ drives, leading to larger supersaturations in P-SPRE. As one might expect, profiles of 90th-percentile differences are similar but with larger values (not shown).

Figure 4 shows profiles of median contributions to the potential density temperature difference between the cloud and the environment (the median potential temperature difference is shown in Fig. 3) for hour 7 of the simulations. As in Fig. 3, all ensemble members are used. Dashed lines show the median D − P difference multiplied by 4 to fit the scale. Figure 4 shows that the temperature perturbations provide the largest contribution to the cloud buoyancy, except for the upper troposphere, where ice condensate loading makes a significant contribution as well. The relatively small D − P difference peaks in the lower troposphere and is dominated by the temperature difference. The D − P temperature contribution is positive (negative) when SADJ drives (piggybacks) the flow, in agreement with what one should expect based on the finite supersaturation impact on buoyancy documented in Fig. 2.

Figures 5 and 6 show histograms of the vertical velocity in the format of Fig. 11 in GM16 for levels in the lower and middle (3- and 5-km heights) and middle and upper (7- and 11-km heights) troposphere and for all time levels during hours 7 and 8. Large panels show histograms constructed from all ensemble members, whereas small panels show whether the difference between D-SADJ and D-SPRE is statistically significant. In general, two

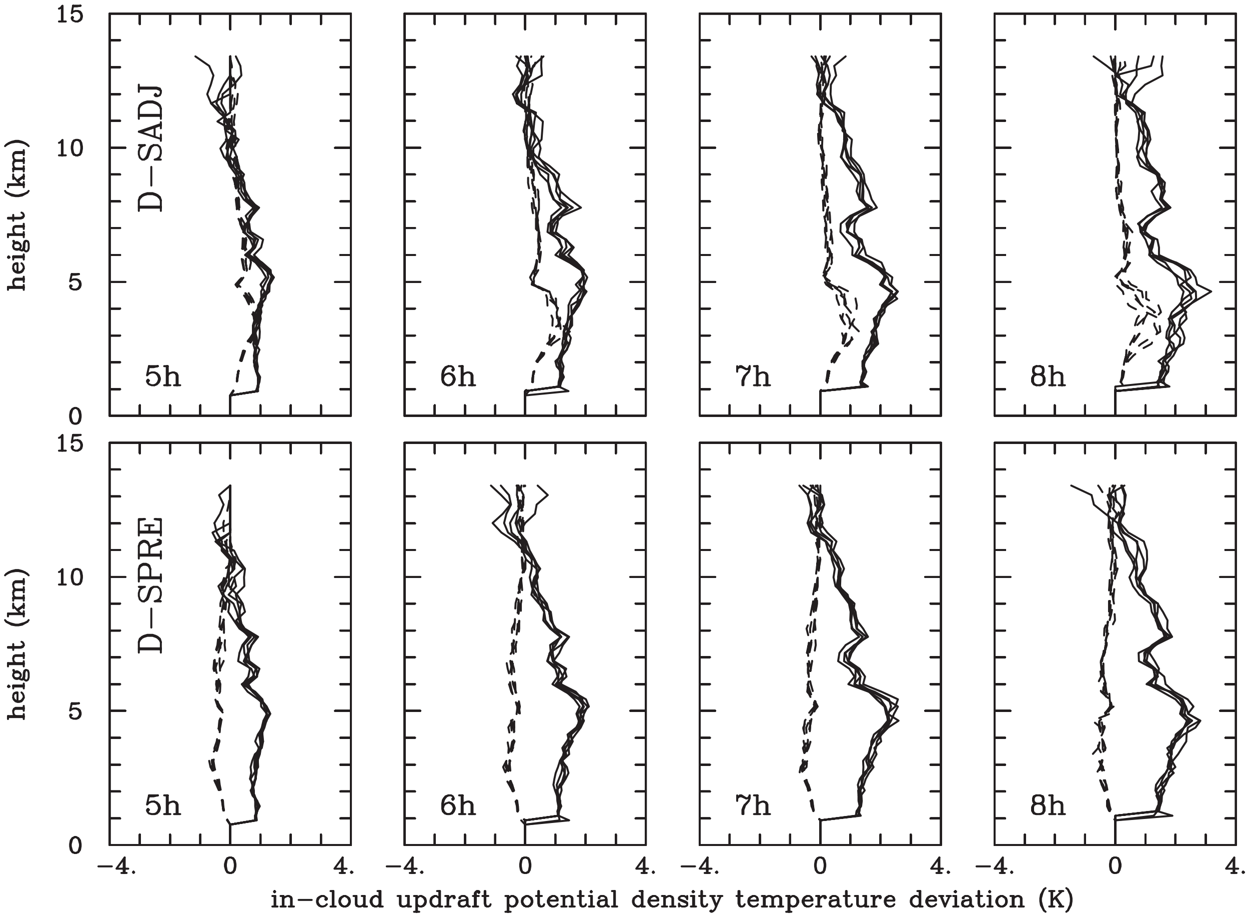

FIG. 3. Profiles of the median density temperature difference between the cloud and its environment for hours 5, 6, 7, and 8 (solid lines) for driving sets [(top) SADJ and (bottom) SPRE] conditionally sampled for points with $w > 1\,\mathrm{m\,s^{-1}}$ and the sum of cloud water and ice larger than $0.1\,\mathrm{g\,kg^{-1}}$. Dashed lines show the median D − P difference multiplied by 4 to fit the scale.

ensembles are statistically different at the 95% confidence level (i.e., confidence interval around 2.3 for the 8 degrees of freedom of the two ensembles) if the Student's *t* test statistic is larger than approximately 1.0: that is, the difference of the mean is larger than the mean standard deviation (the latter calculated as the square root of the sum of the squared standard deviations from the two five-member ensembles; the standard deviation for a given ensemble member refers here to the deviation from the mean for all time levels for hours 7 and 8). The asterisks in the small panels show the ratio between the mean standard deviation and the difference between the mean values. Thus, if the star is between the dotted lines (showing the −1 and +1 values), then the difference between D-SAD and D-PRE is statistically significant at the 95% confidence level.

The histograms at the heights of 3 and 5 km (Fig. 5) extend to about $15\,\mathrm{m\,s^{-1}}$. For updrafts stronger than about $5\,\mathrm{m\,s^{-1}}$, there is a statistically significant difference between SADJ and SPRE, with SADJ bins showing larger counts. This is consistent with larger cloud buoyancy when water supersaturations are not allowed. For updrafts in the 3–$5\,\mathrm{m\,s^{-1}}$ range, SPRE seems to have a statistically significant larger number of counts, perhaps more difficult to explain. At higher levels (7 and 11 km; Fig. 6), the statistics extend to stronger updrafts (around $20\,\mathrm{m\,s^{-1}}$), and a statistically significant larger number of counts is present for SADJ, as one might expect.

b. *Macroscopic cloud and precipitation characteristics*

Figure 7 (in the format to be used for other simulations) shows the key macrophysical outcomes from the D-SPRE/P-SADJ and D-SADJ/P-SPRE ensembles. The top two rows show the evolution of the cloud fraction profiles for hours 2, 4, 6, 8, 10, and 12, with SADJ and SPRE driving in first row and second row, respectively. As in all subsequent figures, solid (dashed) lines show results from the driver (piggybacker). The cloud fraction at any level is defined as the fraction of grid points at that

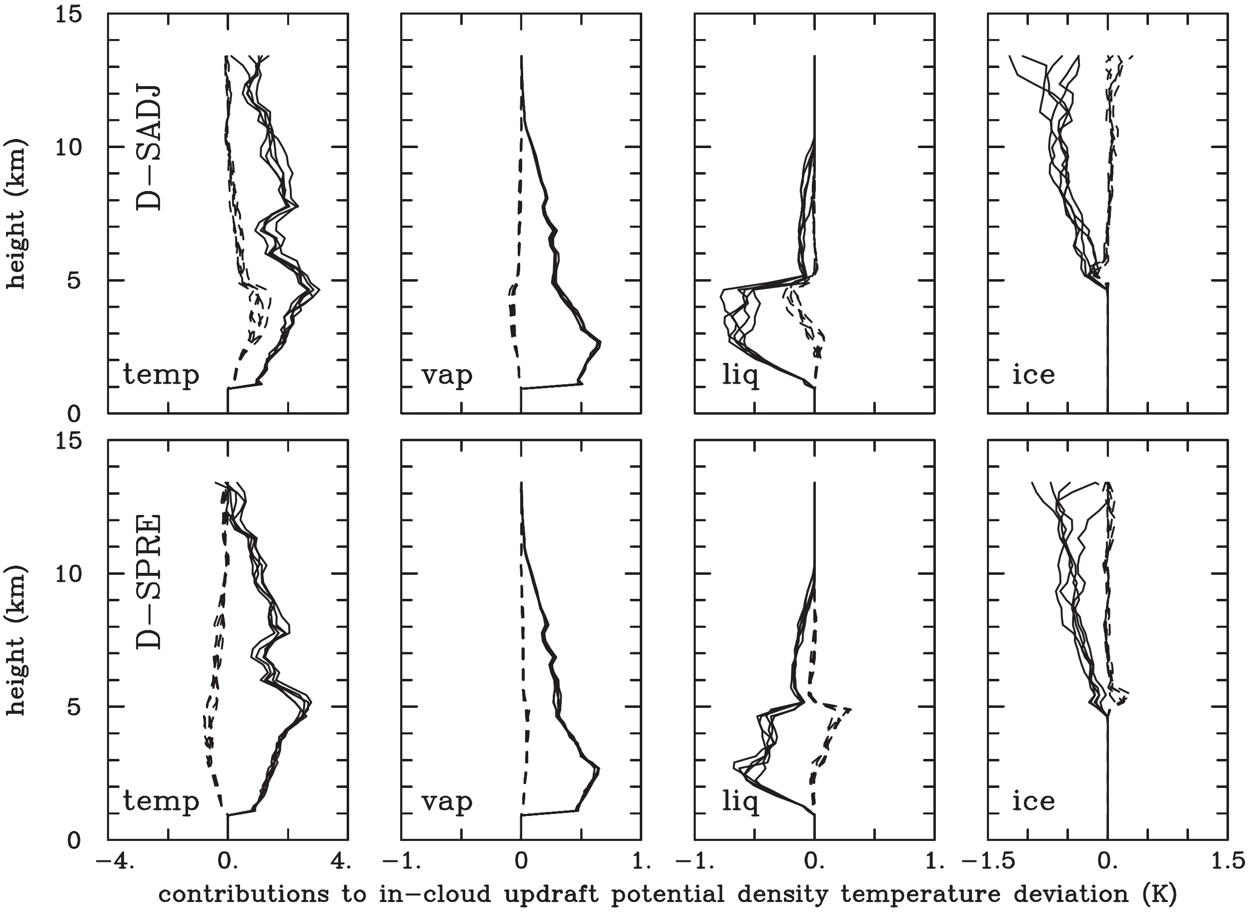

FIG. 4. Median contributions to the in-cloud updraft density potential temperature difference between the cloud and its environment shown in Fig. 3 due to (left)–(right) temperature (temp), water vapor (vap) liquid water (liq), and ice water (ice) for hour 7 for the entire ensemble of simulations. Note different scale on horizontal axis in different panels. Dashed lines show the median D − P difference multiplied by 4 to fit the scale.

level with the sum of the cloud water and total ice mass mixing ratios larger than 0.01 g kg^{-1}, as in GM16. Left panels in the bottom part of the figure show the evolution of the surface total rain accumulations, and the evolution of the D − P difference (i.e., solid minus dashed lines in the left panels) is shown in the right panel.

The cloud fraction panels show the typical convective development in the LBA case: no clouds at the onset, only shallow convection at hours 2 and 4 (barely noticeable for hour 2 in the figure), transition to deep convection between hours 4 and 6, and only convective anvils at hour 12. As in Grabowski (2015) and GM16, individual simulations document the need for an ensemble approach for these relatively small horizontal domain runs. The differences between sets D and P of thermodynamic variables are relatively small until significant upper-tropospheric anvils develop in the second half of the simulation. In general, SPRE has significantly higher anvil cloud fractions regardless of whether they drive (second row) or piggyback (first row) the simulation. Since SPRE members have weaker updraft velocities as a result of significant supersaturations, an aspect quantified previously, higher anvil cover in SPRE cases is surprising. This aspect will be explored through sensitivity simulations discussed in section 4. Larger anvil fractions when SADJ drives (first row) compared to when SPRE drives (second row) are consistent with stronger updrafts in the SADJ cases.

The bottom panels show that SADJ simulations have about 3% more rain accumulation regardless of which set drives the simulation. Since SADJ features larger droplet concentrations below the 0°C level compared to SPRE (to be documented in Fig. 8), higher surface rain accumulation suggests that the D − P difference comes not from warm rain but rather from ice processes. There is still a noticeable increase in the D − P difference (right panel) when SADJ is driving, but not as large as in the polluted versus pristine accumulations in GM16 (see their

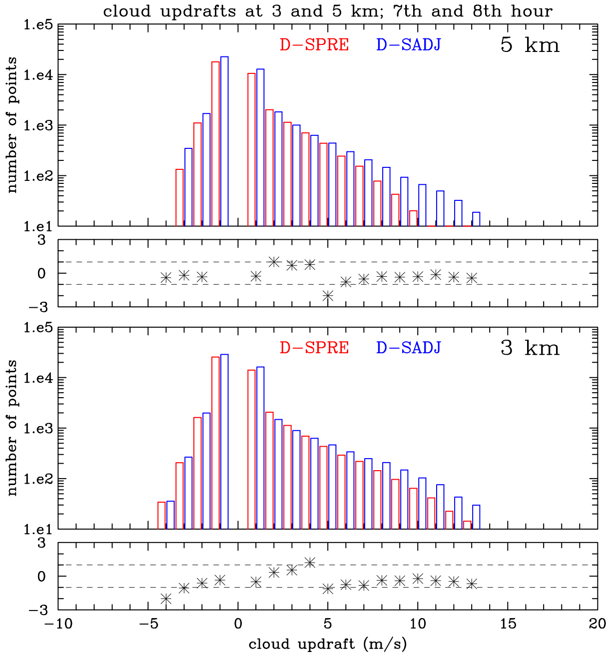

FIG. 5. Histograms of the vertical velocity at (top) 3 and (bottom) 5 km for hours 7 and 8 in simulations driven by SPRE and SADJ sets of the thermodynamic variables. Bin size is 1 m s^{-1} and two bars are shown for each bin: one for SPRE (red color) and one for SADJ (blue). Also shown is the statistical significance of the difference between SPRE and SADJ vertical velocity in each bin. The difference in the updraft statistics is statistically significant if the asterisk is between the dashed lines. An asterisk located above (below) the zero line implies that SPRE minus SADJ for this bin is positive (negative).

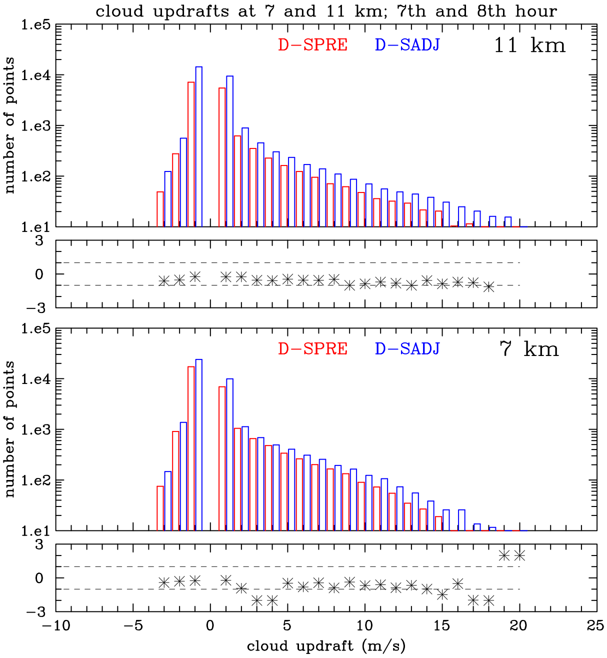

FIG. 6. As in Fig. 5, but for heights of 7 and 11 km.

Figs. 6 and 12). There is also slightly more rain accumulation for SPRE for the shallow convection phase (i.e., before hour 4; note that the difference lines cross the zero line around hour 5 in the bottom right panel), arguably because of lower average droplet concentrations in SPRE (see Fig. 8) and instantaneous cloud water evaporation near cloud edges in SADJ cases (see discussion in GJ15).

c. Microphysical cloud and precipitation characteristics

Figures 8 and 9, in the format of Fig. 4 in GM16, show conditionally sampled cloud and precipitation profiles averaged for all time levels saved to the output files for hours 7 and 8 and for all drivers and piggybackers from all ensemble members of D-SPRE/P-SADJ and D-SADJ/P-SPRE simulations. Figure 8 shows profiles of mean conditionally sampled fields including all volumes with cloud water mixing ratio larger than 0.01 g kg^{-1} for cloud, drizzle/rainwater larger than 0.001 g kg^{-1}, and the total ice mixing ratio larger than 0.001 g kg^{-1}. Figure 9 shows similar profiles, but with additional restriction of updraft velocity larger than 10 m s^{-1}. However, the number of conditional sampling data points in Fig. 9 rapidly decreases with height in the upper troposphere. It is below 100 above 15 km, compared to over 2000 at 10 km for each ensemble. We only show statistics for the period of the most vigorous convection, as they best illustrate the origin of the key differences between SPRE and SADJ.

The key results shown in Fig. 8 can be summarized as follows. Cloud droplet number mixing ratios for temperatures below −40°C are higher for the SADJ regardless of if it drives or piggybacks the flow. This comes from larger vertical velocity (on which CCN activation is based) in SADJ cases. The differences extend well above the 0°C layer where ice processes become progressively more important moving to lower temperatures. The drizzle/rainwater mixing ratios do not vary significantly between SADJ and SPRE below the 0°C layer, but there are some noticeable differences higher up. The large maxima of the rain number and mass mixing ratios arguably comes from melting of solid precipitation falling from above.[1] The differences between

---

[1] For simplicity, the 0° and −40°C levels shown in the figure are based on the initial temperature profile. Using the predicted horizontally averaged temperature profile changes these levels little, while conditionally sampling using varying rain or cloud water mass mixing ratio thresholds leads to varying increases in the heights of these levels. This explains why cloud water appears at temperatures colder than the homogeneous freezing level and also likely explains why the rainwater maximum occurs just above the 0°C level.

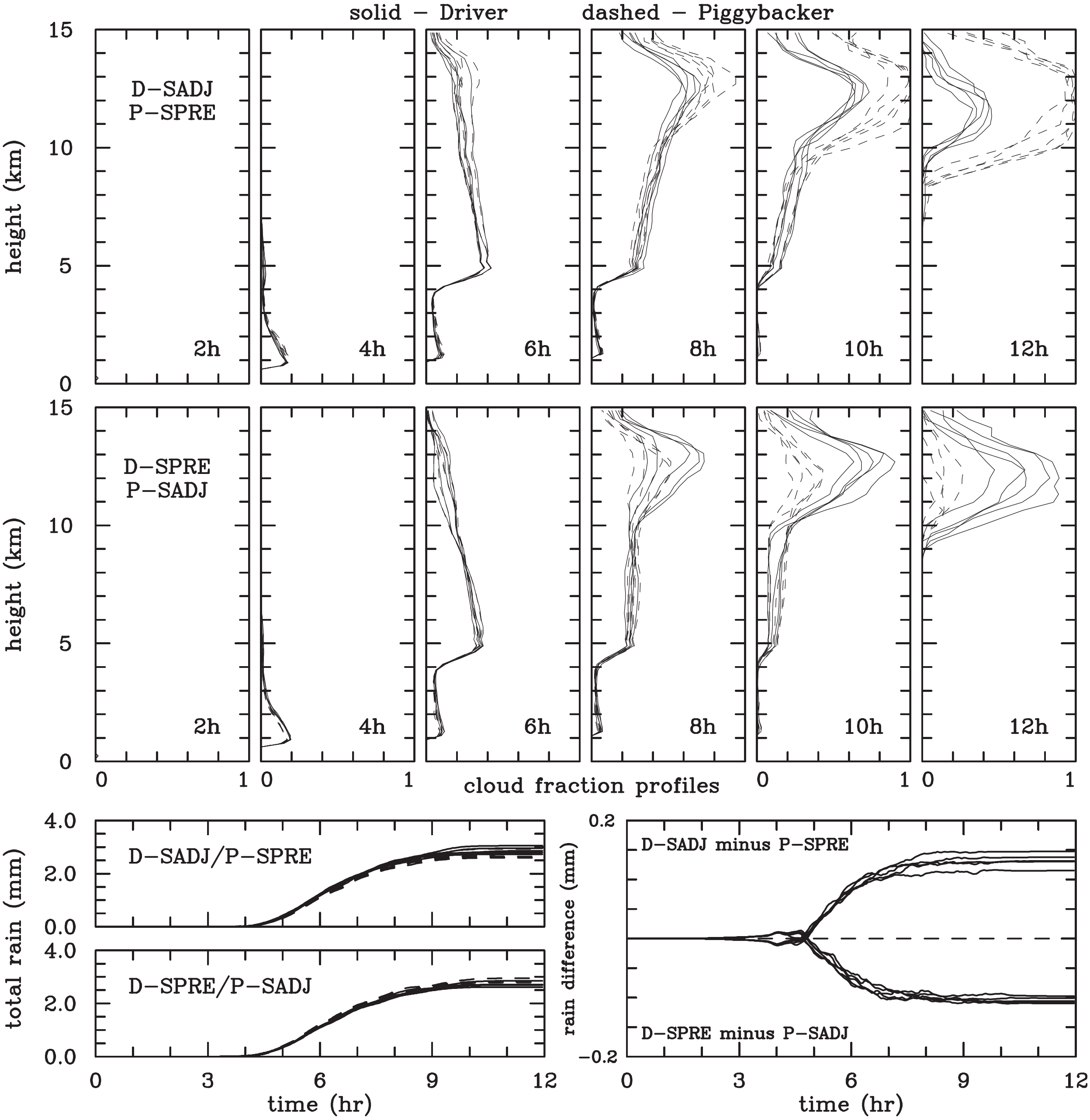

FIG. 7. (top),(middle) Evolutions of the cloud fraction profiles for five members of (top) D-SADJ/P-SPRE and (middle) D-SPRE/P-SADJ piggybacking simulations for hours 2, 4, 6, 8, 10, and 12 as marked. (bottom) Corresponding evolutions of (left) total rain accumulations and (right) evolutions of the D − P differences. Solid (dashed) lines are for thermodynamic sets driving (piggybacking) the simulated flow.

SADJ and SPRE are similar between the left and right panels. The ice number mixing ratio increases almost linearly with height on the log-linear plot, with values up to several thousand per gram (i.e., approximately per liter) at tops of the anvils. The ice number mixing ratios in SPRE sets are significantly higher in both D-SPRE/P-SADJ and D-SADJ/P-SPRE simulations. Since the ice mass mixing ratios are similar above the homogeneous freezing level in SPRE and SADJ, the simulated mean ice particle mass is smaller in SPRE, and thus it has smaller sedimentation velocity. This is consistent with significantly higher anvil cloud fractions for SPRE late in the simulations, as documented in Fig. 7.

When averaged only over cloud updrafts stronger than 10 m s^{-1} (Fig. 9), the SADJ and SPRE differences

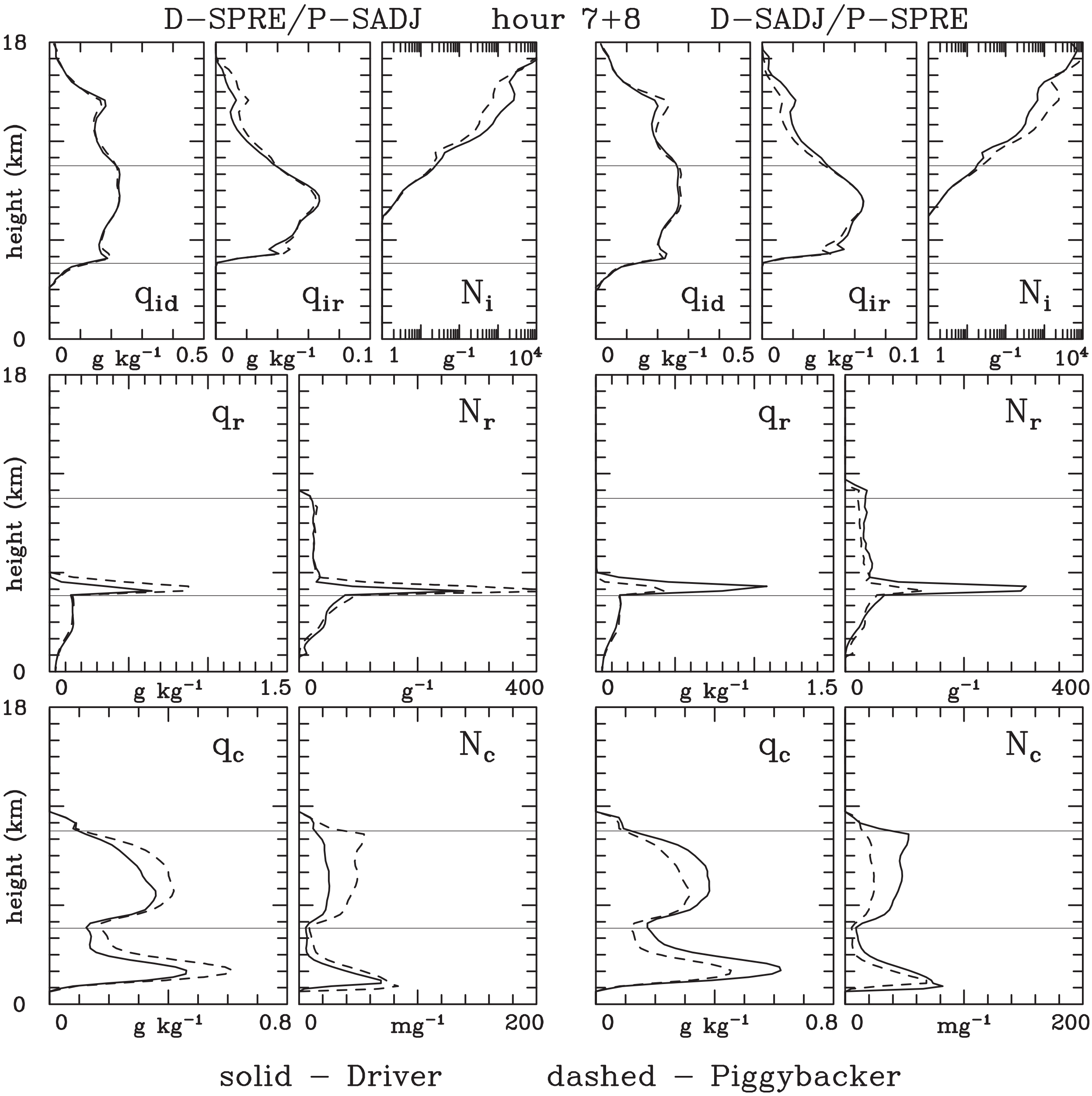

FIG. 8. Profiles of conditionally sampled cloud, rain, and ice fields for all ensemble members and for all 20 time levels during hours 7 and 8 of the simulation (left) D-SPRE/P-SADJ and (right) D-SADJ/P-SPRE. Solid (dashed) lines are sets driving (piggybacking) the flow. Horizontal lines show approximate heights of 0° and −40°C based on the initial sounding.

are smaller. However, the actual mass and number mixing ratios are much larger than shown in Fig. 8 because such strong updrafts are no doubt only weakly diluted by entrainment. High ice number mixing ratios in the upper troposphere, similar in amplitude to the lower-tropospheric cloud droplet mixing ratios, come from homogeneous freezing of cloud and (arguably to a smaller extent) drizzle and raindrops. In contrast to the profiles shown in Fig. 8, the ice mass mixing ratio grown by riming is similar in magnitude to the mass grown by diffusion of water vapor.

Figures 10 and 11 show scatterplots of the supersaturation in the SADJ set, local vertical velocity, and number mixing ratio of activated CCN as a function of the supersaturation in SPRE set, the latter driving the simulation in the left panels or piggybacking in the right panels. The data come from hour 7 of the simulation, with Figs. 10 and 11 showing statistics at heights of 3 and 9 km,

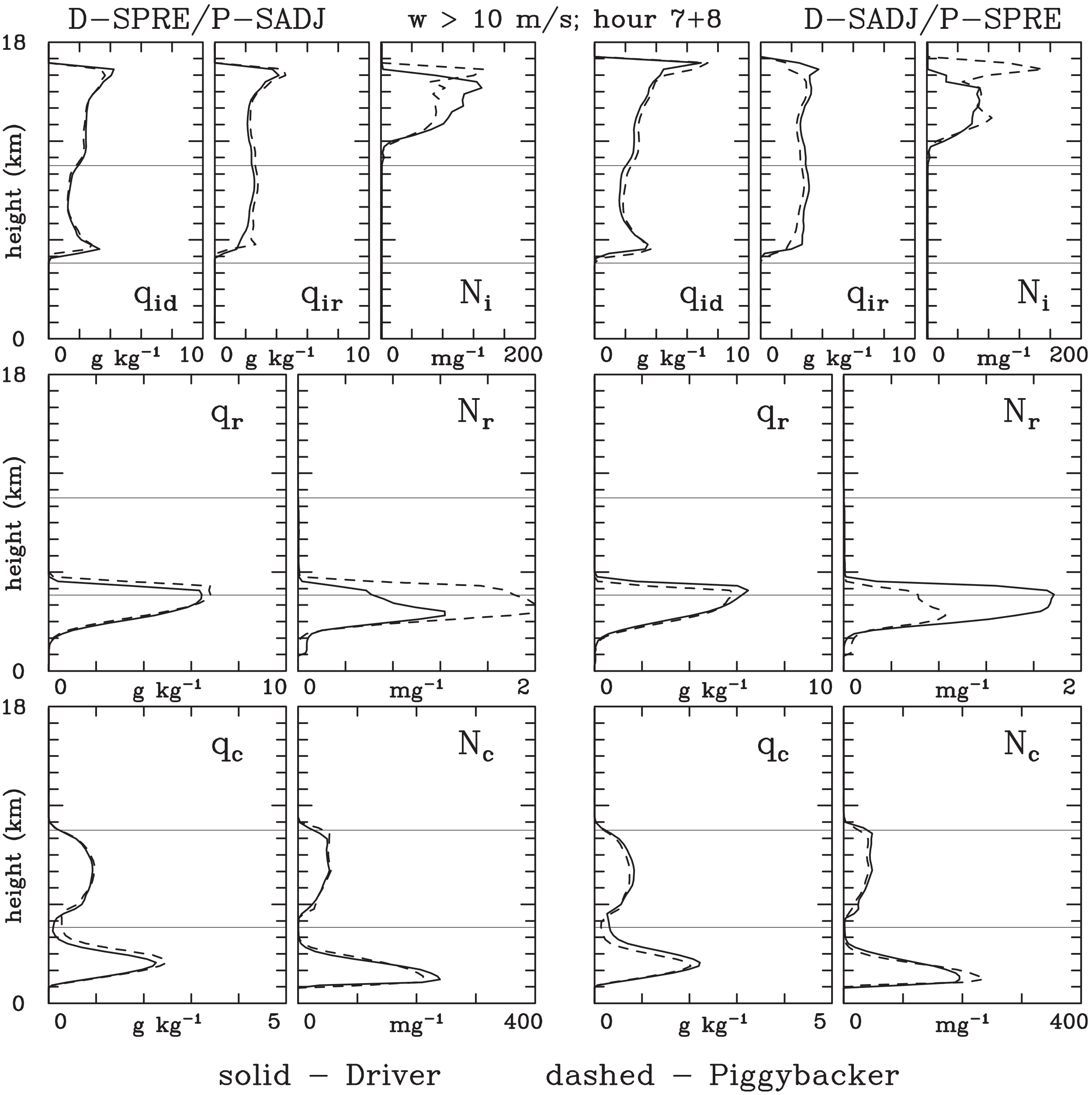

FIG. 9. As in Fig. 8, but only for grid points with updraft velocity larger than 10 m s^{-1}. Note different scales on horizontal axes in most of the panels compared to Fig. 3.

respectively. We first note that supersaturations in SADJ are approximately zero, as they should be, confirming that the saturation adjustment works correctly. Second, supersaturations in SPRE are large, up to 10% and larger (and larger at 9 than 3 km), and they are associated with strong updrafts (up to 13 m s^{-1} at 3 km and 18 m s^{-1} at 9 km) and typically significant precipitation. These values are consistent with simulation results of Hall (1980), as discussed in GM16 (see the right column on p. 3767), and the quasi-equilibrium supersaturations as discussed later (cf. Fig. 15), similar to the pristine versus polluted simulations presented in GM16 (see Fig. 9 therein). Finally, the number mixing ratio of activated CCN increases with the updraft velocity in a manner similar to the activation parameterization (cf. Fig. 1).

d. Summary

The results presented above document a modest dynamical impact and a large microphysical impact when saturation adjustment is applied in the microphysical

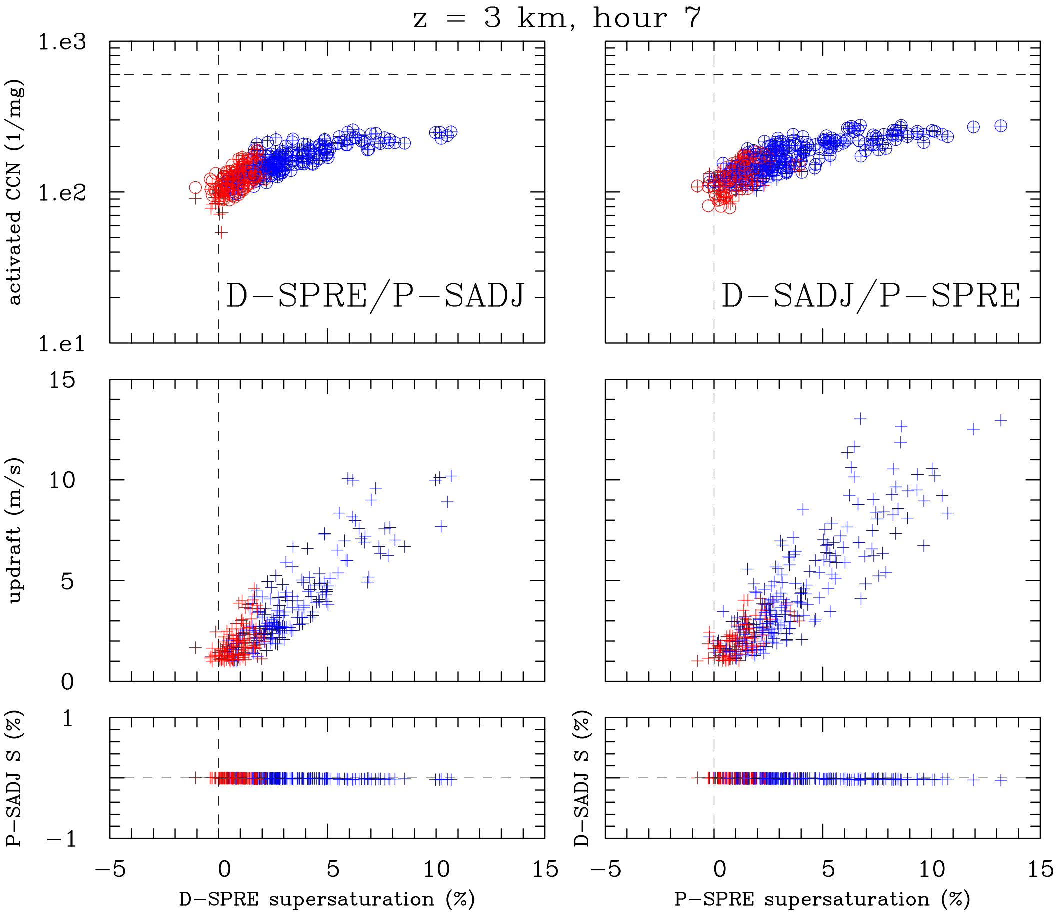

FIG. 10. (bottom) Supersaturation in the SADJ set of thermodynamic variables, (middle) updraft velocity, and (top) concentration of the activated CCN in (left) D-SPRE/P-SADJ and (right) D-SADJ/P-SPRE simulations. Pluses (circles) are for driver (piggybacker) in (top). Data at $t = 7$ h and $z = 3$ km. Only points with $q_c > 0.1$ g kg^{-1} are included. Red (blue) color marks points with precipitation (i.e., rain plus snow) mixing ratio smaller (larger) than 1 g kg^{-1}.

scheme. Note that the dynamical and microphysical impacts seem to work in the opposite directions. On one hand, stronger updrafts with SADJ as the driver suggest that more cloud mass can be transported into the upper troposphere, which should lead to a larger anvil coverage. On the other hand, smaller ice concentrations together with similar ice mass mixing ratios in SADJ imply larger ice particle and thus larger sedimentation rates that lead to a smaller anvil coverage. However, despite the differences in updraft statistics discussed above, profiles of the cloud updraft and downdraft mass fluxes differ little regardless of whether SADJ and SPRE is the driver (not shown), and overall the microphysical impact dominates. Sensitivity simulations that further support these conclusions are discussed in the next section.

4. Sensitivity simulations

In this section, additional piggybacking simulations are discussed to better understand the differences between SPRE and SADJ. The methodology is to systematically change elements of the microphysics to bring the SPRE and SADJ schemes closer to each other. If changing a given part of the model physics brings D and P sets closer to each other, this implies that the modified part of the model plays a significant role in creating the D and P differences in the original simulations. Below, we describe systematic changes and outcomes of sensitivity piggybacking simulations. These simulations will be referred to as SP*xx* (as SPRE with "*xx*" describing additional changes) and SA*xx* (as SADJ with additional changes). Only three members are run for these ensemble sensitivity simulations.

a. *Simulations with constant cloud droplet concentration*

Because of the impact of nonzero in-cloud supersaturations on the buoyancy field and thus on the vertical velocities, simulations SPRE and SADJ result

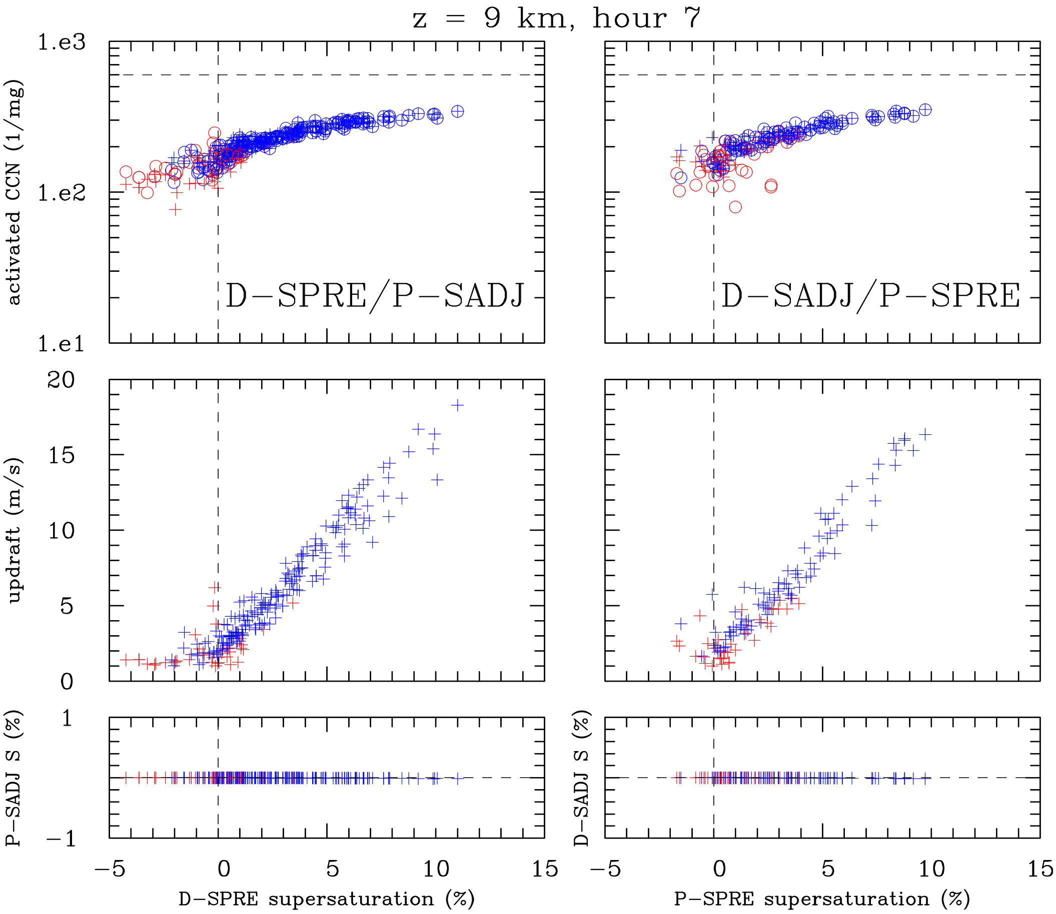

FIG. 11. As in Fig. 10, but at a height of 9 km.

in different cloud droplet concentrations when applying the CCN activation parameterization described in section 2 (see Fig. 8). Thus, the first sensitivity test is to prescribe constant cloud droplet concentrations of 50 mg^{-1} (i.e., around 50 cm^{-3}) in both SPRE and SADJ. The thermodynamic variable sets in piggybacking simulations are referred to as saturation prediction (SP)/saturation adjustment (SA) with constant droplet concentration (NC) (SPNC and SANC). Figure 12, in the format of Fig. 7, shows the impact on the difference between SPNC and SANC. Overall, the differences between Figs. 7 and 12 are relatively small. Of note are the smaller differences between precipitation accumulation between D and P sets (note that the scales on the vertical axes in Fig. 7 are twice as large as in Fig. 12). Having the same droplet concentrations reduces the D − P difference in the surface precipitation. The D − P anvil fractions are similar in SANC/SPNC and SADJ/SPRE ensembles (i.e., saturation adjustment leads to lower anvil fractions during the last 3 h of the simulations regardless of whether it drives or piggybacks the simulation). This implies that the droplet concentration (higher in the SADJ ensemble and assumed constant in the SANC/SPNC ensembles) has only a small role in driving the SADJ/SPRE anvil fraction differences. However, the difference in the anvil fractions in simulations when SADJ drives versus when it piggybacks (i.e., top vs bottom cloud fraction panels) apparent in Fig. 7 is no longer evident in Fig. 12. Updraft statistics are similar between SADJ/SPRE and SANC/SPNC ensembles (i.e., more updrafts in most bins in SANC ensemble; however, the differences are not statistically significant because of the smaller ensemble size).

b. *Simulations with constant cloud droplet concentration and the same ice initiation*

Ice initiation formulation in simulations discussed so far strongly contributes to the D − P differences. This is because the Meyers et al. (1992) ice initiation formulation depends on the ice supersaturation, with the number mixing ratio of ice nuclei (kg^{-1}) given by

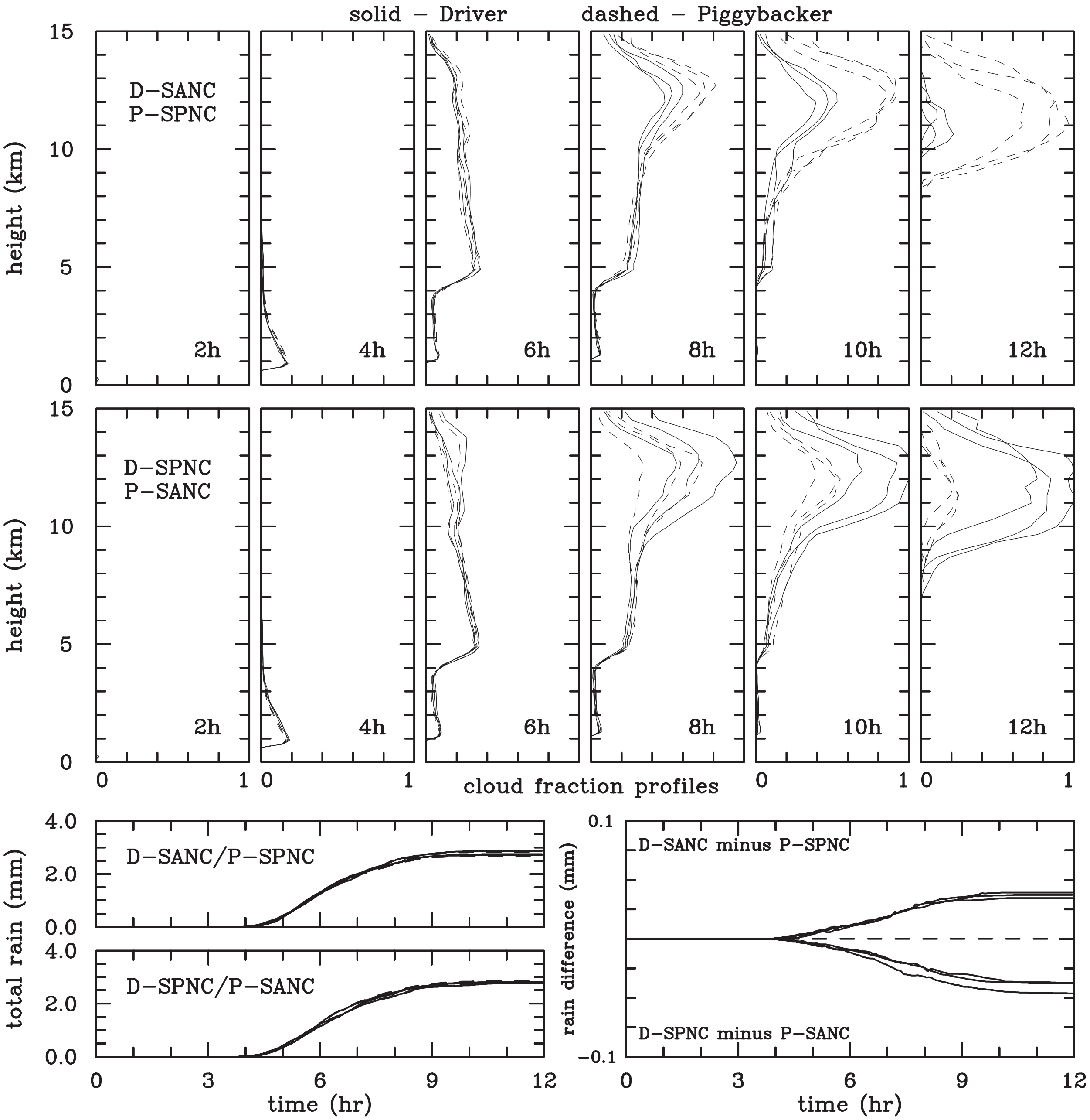

FIG. 12. As in Fig. 7, but for constant droplet concentration piggybacking ensemble SPNC and SANC. Note a different scale on (bottom right) the difference compared to Fig. 2.

$$N_{\mathrm{IN}} = \min\left[\frac{100}{\rho}, \frac{1000}{\rho}\exp(-0.639 + 0.1296S_i)\right], \tag{2}$$

where ρ is the air density and S_i is the supersaturation ratio with respect to ice (%). However, with significant water supersaturations in SPRE (cf. Fig. 11), the ice supersaturations are higher as well. Thus, one should expect higher rates of ice initiation in SPRE that eventually lead to higher anvil fractions. To show that this is the key mechanism, we perform a set of piggybacking simulations where the ice supersaturation-dependent Meyers et al. (1992) ice initiation formulation is replaced by the temperature-dependent Cooper (1986) formulation:

$$N_{\mathrm{IN}} = \min\left\{\frac{100}{\rho}, \frac{5}{\rho}\exp[0.304(273.15 - T)]\right\}, \tag{3}$$

where T is in kelvins. These simulations also assume constant cloud droplet concentration, as in the previous section. The sets of thermodynamic variables are referred to as saturation adjustment with modified ice initiation

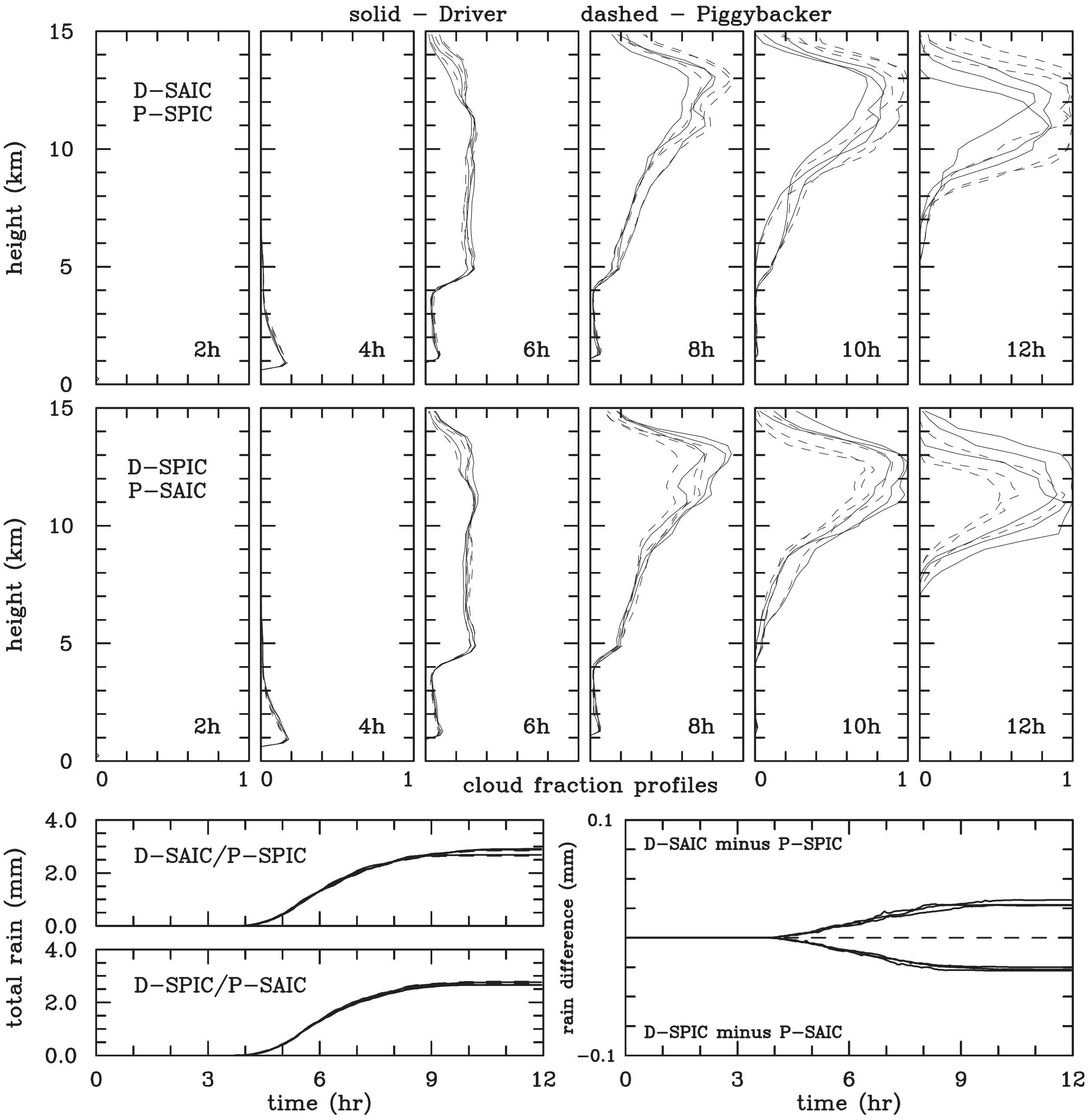

FIG. 13. As in Fig. 7, but for constant droplet concentration and modified ice initiation ensemble SPIC and SAIC.

(SAIC) and saturation prediction with modified ice initiation (SPIC), and the simulations are D-SAIC/P-SPIC and D-SPIC/P-SAIC. Figure 13 shows results of these simulations. Applying the modified ice initiation formulation and a constant cloud droplet concentration has a small impact on the surface precipitation but a large effect on the evolution on upper-tropospheric anvils. The differences between anvil cloud fractions for D and P sets of thermodynamic variables are significantly reduced when compared to previous ensembles. This implies that the lower anvil fractions for the saturation adjustment scheme in SADJ/SPRE ensemble come mainly from higher ice supersaturations in SPRE and thus higher ice initiation rates when the Meyers et al. (1992) scheme is used.

c. Simulations with constant cloud droplet concentration, the same ice initiation, and constant particle fall velocities

The final simulation ensemble assumes constant droplet concentration and modified ice initiation as in

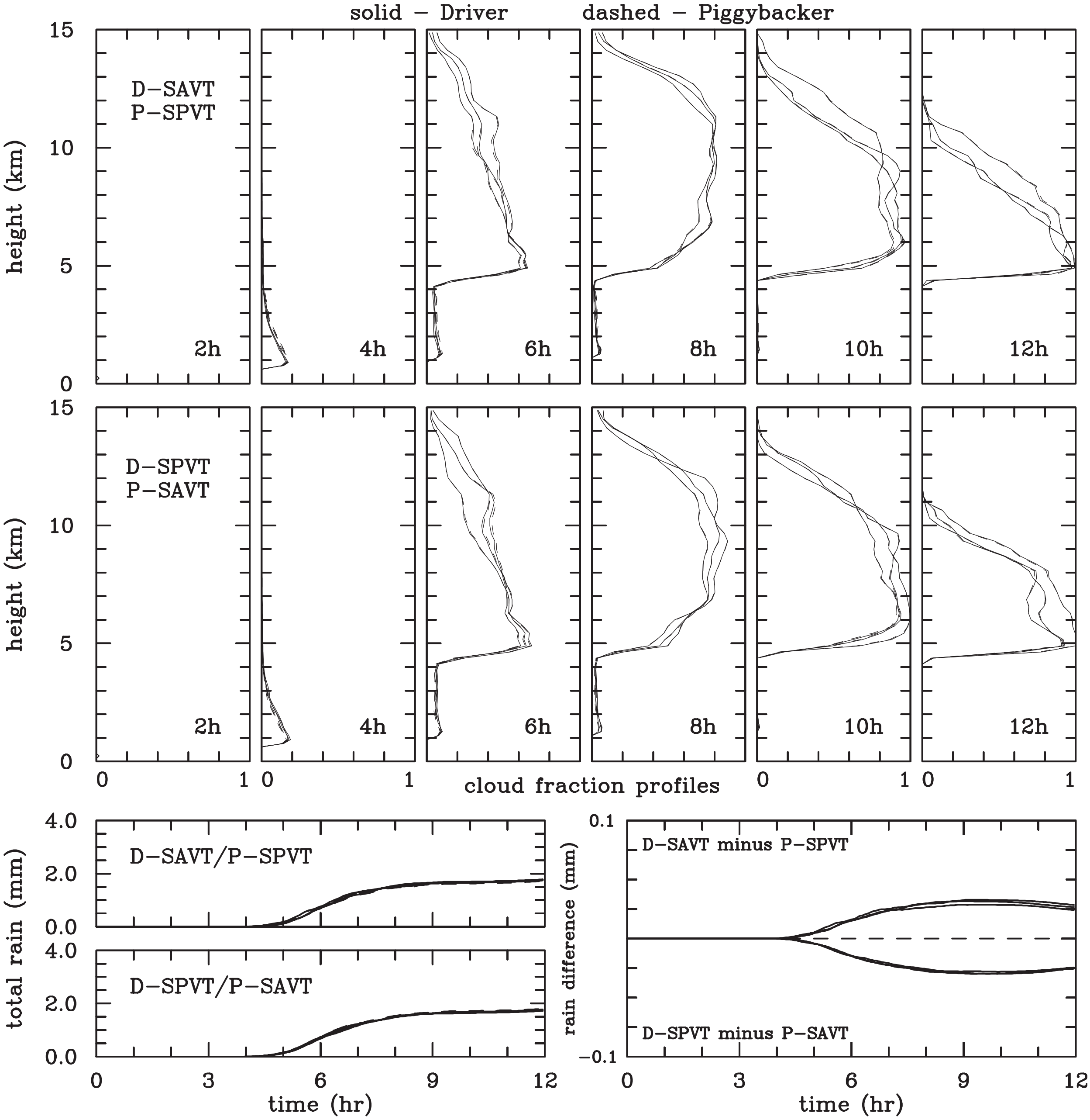

FIG. 14. As in Fig. 7, but for constant droplet concentration, modified ice initiation, and constant sedimentation for cloud and precipitation fields for ensembles SPVT and SAVT. Note that solid and dashed lines in the cloud fraction profiles overlay each other.

the "NC" and "IC" simulations in the two previous sections and adds a constant fall velocity assumption for both water and ice. In these simulations, the sedimentation velocity (mass weighted for mass mixing ratios and number weighted for number mixing ratios and thus different for masses and numbers in addition to being different for cloud droplets, rain, and ice) is assumed to be zero for cloud water number and mass mixing ratios, 5 m s^{-1} for rain mass and number, and 0.5 m s^{-1} the for ice variables. Sets of thermodynamic variables from these simulations are referred to as saturation adjustment with constant sedimentation velocity VT (SAVT) and saturation prediction with constant sedimentation velocity VT (SPVT). Figure 14 shows cloud fractions and surface rain accumulations in the same format as Figs. 7, 12, and 13. As Fig. 14 documents, the impact on the upper-tropospheric anvil fractions is dramatic, as the driver and piggybacker sets are virtually indistinguishable (i.e., the solid and dashed lines overlay each other). The surface rain accumulations are further reduced (bottom-left panels), whereas the D − P differences are similar to previous sensitivity simulations (Figs. 12, 13).

Motivated by the impact on the anvil cloud fractions in these simulations, we also run simulations as with SADJ and SPRE, but with the same sedimentation velocities as in the VT ensembles. The outcome is very similar to SAVT and SPVT, with the solid and dashed lines almost exactly one over another (not shown). This clearly shows that the key difference in the anvil evolution in SADJ/SPRE ensemble is directly tied to the sedimentation velocity of the ice field, with larger anvil fractions at the end of simulations resulting from larger ice concentrations, smaller mean sizes, and lower ice sedimentation in SPRE.

5. Discussion and conclusions

Motivated by large supersaturations inside convective updrafts in simulations of deep unorganized convection contrasting pristine and polluted conditions discussed in GM16, we investigate the impact on deep convection simulations of the saturation adjustment often applied in bulk microphysical schemes. For shallow nonprecipitating convection, this has already been investigated in GJ15. GJ15 simulations show a rather small impact on convective drafts, but a significant reduction of the simulated mean cloud fractions as a result of the instantaneous evaporation of cloud water near cloud edges when saturation adjustment is used (see also Xue and Feingold 2006). Hall (1980) simulated supersaturation values higher than 5% in upper parts of a cloud where updraft velocity exceeded $8\,\mathrm{m\,s^{-1}}$. He argued that such high supersaturations originated from removal of cloud water by precipitation processes and inability of the remaining cloud droplets to absorb water vapor available for diffusional growth in the strong cloud updraft (cf. Figs. 10 and 11 herein). Lebo et al. (2012) showed large supersaturations (several percent and larger) in their supercell simulations applying various microphysical schemes. Large supersaturations in simulated deep convection call for observational support for their existence, either directly (i.e., by combining accurate temperature and water vapor measurements) or indirectly, for instance, by investigating residuals of cloud droplets (i.e., the CCN they formed on) in an attempt to expose their activation history.

We apply the piggybacking methodology (Grabowski 2014, 2015; GJ15; GM16) to separate dynamical and microphysical impacts applying either the saturation adjustment (SADJ) or predicting the supersaturation (SPRE) in the same double-moment microphysical scheme. The dynamical impact comes from large supersaturations in SPRE that reduce cloud buoyancy and thus affect convective dynamics. This is shown to modify updraft statistics, with SADJ featuring stronger updrafts. The impact on the surface precipitation is relatively minor, with SADJ showing a few-percent-larger rain accumulations. The primary microphysical impact concerns ice initiation. Because the Meyers et al. (1992) ice initiation scheme includes a dependence on the ice supersaturation, significant water supersaturations in SPRE also imply larger ice supersaturations and thus higher ice initiation rates. This leads to a significant increase of ice concentrations and significantly higher upper-tropospheric anvil fractions in SPRE. The anvils are left in the upper troposphere after deep convection terminates, with the difference between SPRE and SADJ ensemble members gradually increasing with time.

An updraft invigoration effect of stronger condensation latent heating is manifested in the increased frequency of updraft speeds exceeding $5\,\mathrm{m\,s^{-1}}$ owing to saturation adjustment in contrast with weaker diabatic forcing associated with explicit condensation and saturation prediction (Figs. 5, 6). The supersaturations simulated by the model are large, several percent, especially for relatively large vertical velocities and in volumes with significant precipitation that rapidly removes cloud water (Hall 1980). However, the microphysical impact may be dependent on the assumed CCN characteristics (e.g., as in pristine vs polluted simulations of GM16), on the specific details of the ice initiation, and on details of the ice growth and fallout. GM16 showed that the polluted versus pristine difference in the upper-tropospheric anvil fractions strongly depends on the assumed CCN distribution. We selected the double-peak CCN distribution for which GM16 piggybacking simulations show reduced pristine minus polluted differences compared to simulations with a single CCN mode (i.e., without a small aerosol particle mode). These differences become much larger for the same CCN distribution when SADJ is contrasted with SPRE in simulations applying the ice initiation scheme as described in section 2 together with the bulk ice parameterization of Morrison and Grabowski (2008b) (see Fig. 7 herein and Fig. 12 in GM16). It follows that the microphysical impact between SADJ and SPRE may change when different CCN concentrations, ice initiation schemes, or ice process parameterizations are used. Moreover, the SADJ and SPRE difference may also depend on the degree of convective organization and thus may be different for organized convection (e.g., a squall line). Overall, subsequent studies using

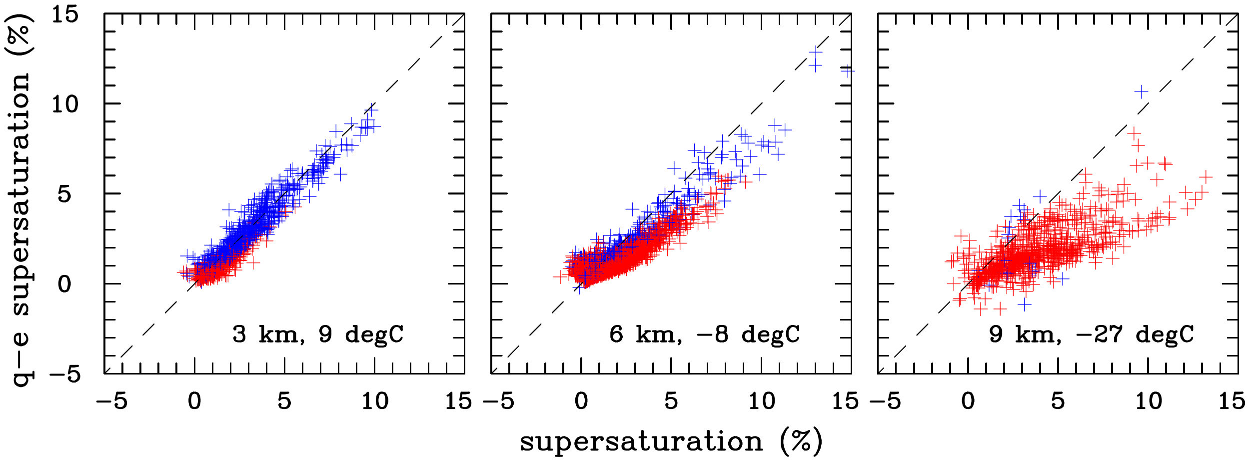

FIG. 15. Scatterplot of the quasi-equilibrium supersaturation calculated as detailed in the appendix vs the actual predicted supersaturation for one member of the ensemble with SPRE driving the simulation and for all output file time levels during the sixth hour of the simulation at heights of approximately (left) 3, (center) 6, and (right) 9 km. Only points with vertical velocity larger than 1 m s^{-1} and cloud water mixing ratio larger than 0.3 g kg^{-1} are included. Red (blue) color corresponds to grid boxes with the phase relaxation time smaller (larger) than 10 s.

models with different representations of cloud microphysics and simulating clouds in different environments are needed to further assess the impact of finite supersaturations on simulated cloud properties.

Sensitivity simulations with fixed water and ice sedimentation velocities document the key role of ice fall velocity in the anvil cloud fraction evolution. This has been pointed out in the past [e.g., Heymsfield et al. (2007) and references therein; Morrison and Grabowski (2011)]. For populations of ice particles in the anvil, a significant issue is the uncertainty of the fall velocity at a given size because of the effects of particle shape and density, rather than how the fall velocity varies across the size distribution. This can be investigated applying a bin microphysics scheme and comparing bulk and bin scheme results using the piggybacking methodology, as done in GJ15 for shallow nonprecipitating convection.

Our results suggest that the numerically efficient scheme based on saturation adjustment may not be appropriate for deep convection simulations. However, the scheme can be improved if the adjustment applies not exactly water saturation conditions, but the quasi-equilibrium supersaturation. The quasi-equilibrium supersaturation corresponds to the exact balance between the source of the supersaturation due to vertical velocity and the sink due to the growth of cloud droplets [e.g., Squires 1952; Politovich and Cooper 1988; see discussion in Grabowski and Wang (2013)]. Such a methodology can also be used in single-moment bulk schemes with assumed cloud and drizzle/raindrop number concentrations as well as in double-moment schemes where the concentrations are predicted. To further motivate such an approach, we present in Fig. 15 a scatterplot of the quasi-equilibrium supersaturation S_{qe} calculated as discussed in the appendix and the actual supersaturation S predicted by the model for all time levels saved to the output files during the sixth hour of the simulation at heights of approximately 3, 6, and 9 km (and corresponding temperatures around 9°, −8°, and −27°C, respectively). Only points with vertical velocity larger than 1 m s^{-1} and cloud water mixing ratio larger than 0.3 g kg^{-1} are included. Red (blue) color marks grid boxes with the phase relaxation time [i.e., as in the dominator in (A5)] smaller (larger) than 10 s. At 3 km (i.e., above freezing), the points are clustered around the 1:1 line. For subfreezing temperatures, the scatter is larger, and the points are no longer clustered around the 1:1 line. The increase of the scatter is perhaps expected because of significantly more complicated thermodynamics when ice processes are involved. However, the decrease of the mean S versus S_{qe} slope with decreasing temperature is intriguing and requires further investigation. Nevertheless, it seems that replacing the $S = 0$ condition with $S = S_{qe}$ in the saturation adjustment procedure for temperature above freezing is justified. For temperatures below freezing, the behavior of the mean slope for the S versus S_{qe} relationship needs to be understood first, and then it can perhaps be used in an improved saturation adjustment procedure. We plan to explore the feasibility of such a method in a future investigation.

Acknowledgments. This work was partially supported by the U.S. DOE ASR Grant DE-SC0016476. WWG was also partially supported by the Polish National Science Center (NCN) "POLONEZ 1" Grant 2015/19/P/ST10/02596. The POLONEZ 1 grant has received funding from the European Union's Horizon 2020 Research and Innovation Program under the Marie Sklodowska-Curie Grant Agreement 665778.

APPENDIX

The Quasi-Equilibrium Supersaturation

The purpose of this appendix is to briefly describe the quasi-equilibrium supersaturation calculations discussed in section 5 and modifications to the double-moment microphysics scheme of Morrison and Grabowski (2007, 2008a,b) (MG scheme). A key aspect of the MG scheme is the prediction of supersaturation. This approach solves the supersaturation evolution and condensation/evaporation rates using quasi-analytic solutions, allowing for numerical stability even with long time steps [see Morrison and Grabowski (2008a) for details]. Predicting the supersaturation, rather than diagnosing it from the predicted potential temperature and water vapor mixing ratio, also allows for the mitigation of cloud-edge supersaturation fluctuations using the technique described in Grabowski and Morrison (2008). The predicted supersaturation approach was extended to the ice phase, as described in Morrison and Milbrandt (2015) [see (C1)–(C7) therein] (see also Korolev and Mazin 2003).

The supersaturation equation when cloud, rain, and ice hydrometeors are present is

$$\frac{d\delta}{dt} = \left(\frac{dq_v}{dt}\right)_{\text{phy}} - \frac{dq_s}{dT}\left(\frac{dT}{dt}\right)_{\text{phy}} - \frac{q_s \rho g w}{p - e_s} + \frac{gw}{c_p}\frac{dq_s}{dT} - \frac{\delta}{\tau_c} - \frac{\delta}{\tau_r} - \left(1 + \frac{L_s}{c_p}\frac{dq_s}{dT}\right)\frac{\delta_i}{\tau_i \Gamma_i}, \tag{A1}$$

where $\delta = q_v - q_s$ is the absolute supersaturation, q_v is the water vapor mixing ratio, e_s and q_s are, respectively, the saturation vapor pressure and saturation mixing ratio (both with respect to water), t is time, ρ is the air density, p is air pressure, g is the gravitational acceleration, c_p is the specific heat of air at constant pressure, w is the vertical velocity, T is the temperature, L_s is the latent heat of sublimation, $\Gamma_i = 1 + (L_s/c_p)(dq_{si}/dT)$, where q_{si} is the saturation mixing ratio with respect to ice, δ_i is the absolute supersaturation with respect to ice, and τ_c, τ_r, and τ_i are the supersaturation relaxation time scales associated with growth of cloud droplets, rain, and ice, respectively. Here $(dq_v/dt)_{\text{phy}}$ and $(dT/dt)_{\text{phy}}$ are the time tendencies of q_v and T due to physical processes other than condensation, evaporation, deposition, and sublimation (e.g., subgrid-scale mixing and radiation). Note that in the simulations presented herein the explicit subgrid-scale mixing and radiation are excluded. Nonetheless, we retain $(dq_v/dt)_{\text{phy}}$ in (A1) for generality.

Solving (A1) requires knowledge of the vertical velocity w field. In (A1) w should be consistent with evolution of the temperature field through adiabatic expansion/compression. Since potential temperature θ is the predicted thermodynamic variable in the model rather than temperature, the adiabatic expansion/compression is not explicitly calculated and is instead implicit in the vertical advection of θ. Given the typically complicated form of higher-order advection schemes, it may not be obvious what value of w in (A1) is consistent with the vertical advection of θ. This issue may be particularly important near cloud edges where the thermodynamic and w fields often have sharp spatial gradients.

To address this issue and improve consistency, we use a new approach for the simulations herein and in GM16, derived as follows. First, consider the equations for temperature and potential temperature written in flux form for the anelastic system:

$$\frac{\partial T}{\partial t} + \frac{1}{\rho_0}\nabla \cdot (\rho_0 \mathbf{u} T) = -\frac{g}{c_p} w + S_H \quad \text{and} \tag{A2}$$

$$\frac{\partial \theta}{\partial t} + \frac{1}{\rho_0}\nabla \cdot (\rho_0 \mathbf{u} \theta) = \frac{S_H}{\Pi}, \tag{A3}$$

where $\mathbf{u}$ is the wind vector, S_H is the temperature change from all physical processes, Π is the Exner function (nondimensional pressure), and ρ_0 is the base-state air density in the anelastic system that is horizontally homogeneous but varies with height . The Exner function Π only varies with height in this model, implying that $\partial T/\partial t = \Pi \partial\theta/\partial t$. However, because there are unavoidable truncation errors when calculating advection, in general $\nabla \cdot (\rho_0 \mathbf{u} T) \neq \Pi \nabla \cdot (\rho_0 \mathbf{u} \theta)$ for the set of discretized model equations. Dividing (A2) by Π, subtracting (A3), eliminating the $\partial/\partial t$ terms using $\partial T/\partial t = \Pi \partial\theta/\partial t$, and rearranging terms gives

$$w = \frac{c_p}{g\rho_0}[\Pi \nabla \cdot (\rho_0 \mathbf{u} \theta) - \nabla \cdot (\rho_0 \mathbf{u} T)]. \tag{A4}$$

This equation provides values of w for the supersaturation equation that are consistent with the evolution of

θ. This w is diagnosed from (A4) using the advection of T and θ at each time step calculated by the model, and applied in solutions of the supersaturation equation and condensation/evaporation rate.

The quasi-equilibrium supersaturation discussed in section 5 and shown in Fig. 15 is derived from (A1) with the assumption that $d\delta/dt = 0$. Rearranging terms gives

$$S_{qe} = \frac{\delta_{qe}}{q_s} = \frac{1}{q_s}\left[\frac{\left(\dfrac{dq_v}{dt}\right)_{\text{phy}} - \dfrac{dq_s}{dT}\left(\dfrac{dT}{dt}\right)_{\text{phy}} - \dfrac{q_s \rho g w}{p - e_s} + \dfrac{gw}{c_p}\dfrac{dq_s}{dT} - \left(1 + \dfrac{L_s}{c_p}\dfrac{dq_s}{dT}\right)\dfrac{(q_s - q_{si})}{\Gamma_i \tau_i}}{\tau_c^{-1} + \tau_r^{-1} + (\Gamma_i \tau_i)^{-1}\left(1 + \dfrac{L_s}{c_p}\dfrac{dq_s}{dT}\right)}\right]. \tag{A5}$$

REFERENCES

Abdul-Razzak, H., and S. J. Ghan, 2000: A parameterization of aerosol activation: 2. Multiple aerosol types. *J. Geophys. Res.*, **105**, 6837–6844, doi:10.1029/1999JD901161.

Bigg, E. K., 1953: The supercooling of water. *Proc. Phys. Soc.*, **B66**, 688–694, doi:10.1088/0370-1301/66/8/309.

Clark, T. L., 1973: Numerical modeling of the dynamics and microphysics of warm cumulus convection. *J. Atmos. Sci.*, **30**, 857–878, doi:10.1175/1520-0469(1973)030<0857:NMOTDA>2.0.CO;2.

Cohard, J.-M., and J.-P. Pinty, 2000: A comprehensive two-moment warm microphysical bulk scheme. I: Description and tests. *Quart. J. Roy. Meteor. Soc.*, **126**, 1815–1842, doi:10.1256/smsqj.56613.

Cooper, W. A., 1986: Ice initiation in natural clouds. *Precipitation Enhancement—A Scientific Challenge, Meteor. Monogr.*, No. 43, Amer. Meteor. Soc., 29–32.

Cotton, W. R., and Coauthors, 2003: RAMS 2001: Current status and future directions. *Meteor. Atmos. Phys.*, **82**, 5–29, doi:10.1007/s00703-001-0584-9.

Ferrier, B. S., 1994: A double-moment multiple-phase four-class bulk ice scheme. Part I: Description. *J. Atmos. Sci.*, **51**, 249–280, doi:10.1175/1520-0469(1994)051<0249:ADMMPF>2.0.CO;2.

Grabowski, W. W., 1989: Numerical experiments on the dynamics of the cloud–environment interface: Small cumulus in a shear-free environment. *J. Atmos. Sci.*, **46**, 3513–3541, doi:10.1175/1520-0469(1989)046<3513:NEOTDO>2.0.CO;2.

——, 1998: Toward cloud resolving modeling of large-scale tropical circulations: A simple cloud microphysics parameterization. *J. Atmos. Sci.*, **55**, 3283–3298, doi:10.1175/1520-0469(1998)055<3283:TCRMOL>2.0.CO;2.

——, 1999: A parameterization of cloud microphysics for long-term cloud-resolving modeling of tropical convection. *Atmos. Res.*, **52**, 17–41, doi:10.1016/S0169-8095(99)00029-0.

——, 2014: Extracting microphysical impacts in large-eddy simulations of shallow convection. *J. Atmos. Sci.*, **71**, 4493–4499, doi:10.1175/JAS-D-14-0231.1.

——, 2015: Untangling microphysical impacts on deep convection applying a novel modeling methodology. *J. Atmos. Sci.*, **72**, 2446–2464, doi:10.1175/JAS-D-14-0307.1.

——, and P. K. Smolarkiewicz, 2002: A multiscale anelastic model for meteorological research. *Mon. Wea. Rev.*, **130**, 939–956, doi:10.1175/1520-0493(2002)130<0939:AMAMFM>2.0.CO;2.

——, and H. Morrison, 2008: Toward the mitigation of spurious cloud-edge supersaturation in cloud models. *Mon. Wea. Rev.*, **136**, 1224–1234, doi:10.1175/2007MWR2283.1.

——, and L.-P. Wang, 2013: Growth of cloud droplets in a turbulent environment. *Annu. Rev. Fluid Mech.*, **45**, 293–324, doi:10.1146/annurev-fluid-011212-140750.

——, and D. Jarecka, 2015: Modeling condensation in shallow nonprecipitating convection. *J. Atmos. Sci.*, **72**, 4661–4679, doi:10.1175/JAS-D-15-0091.1.

——, and H. Morrison, 2016: Untangling microphysical impacts on deep convection applying a novel modeling methodology. Part II: Double-moment microphysics. *J. Atmos. Sci.*, **73**, 3749–3770, doi:10.1175/JAS-D-15-0367.1.

——, and Coauthors, 2006: Daytime convective development over land: A model intercomparison based on LBA observations. *Quart. J. Roy. Meteor. Soc.*, **132**, 317–344, doi:10.1256/qj.04.147.

Hall, W. D., 1980: A detailed microphysical model within a two-dimensional dynamic framework: Model description and preliminary results. *J. Atmos. Sci.*, **37**, 2486–2507, doi:10.1175/1520-0469(1980)037<2486:ADMMWA>2.0.CO;2.

Hallett, J., and S. C. Mossop, 1974: Production of secondary ice particles during the riming process. *Nature*, **249**, 26–28, doi:10.1038/249026a0.

Heymsfield, A., G. van Zadelhoff, D. Donovan, F. Fabry, R. Hogan, and A. Illingworth, 2007: Refinements to ice particle mass dimensional and terminal velocity relationships for ice clouds. Part II: Evaluation and parameterizations of ensemble ice particle sedimentation velocities. *J. Atmos. Sci.*, **64**, 1068–1088, doi:10.1175/JAS3900.1.

Hong, S.-Y., J. Dudhia, and S.-H. Chen, 2004: A revised approach to ice microphysical processes for the bulk parameterization of clouds and precipitation. *Mon. Wea. Rev.*, **132**, 103–120, doi:10.1175/1520-0493(2004)132<0103:ARATIM>2.0.CO;2.

Khain, A., A. Pokrovsky, M. Pinsky, A. Seifert, and V. Phillips, 2004: Simulation of effects of atmospheric aerosols on deep turbulent convective clouds using a spectral microphysics mixed-phase cumulus cloud model. Part I: Model description and possible applications. *J. Atmos. Sci.*, **61**, 2963–2982, doi:10.1175/JAS-3350.1.

Kogan, Y. L., 1991: The simulation of a convective cloud in a 3-D model with explicit microphysics. Part I: Model description and sensitivity experiments. *J. Atmos. Sci.*, **48**, 1160–1189, doi:10.1175/1520-0469(1991)048<1160:TSOACC>2.0.CO;2.

Korolev, A. V., and I. P. Mazin, 2003: Supersaturation of water vapor in clouds. *J. Atmos. Sci.*, **60**, 2957–2974, doi:10.1175/1520-0469(2003)060<2957:SOWVIC>2.0.CO;2.

Lebo, Z. J., and J. H. Seinfeld, 2011: Theoretical basis for convective invigoration due to increased aerosol concentration. *Atmos. Chem. Phys.*, **11**, 5407–5429, doi:10.5194/acp-11-5407-2011.

——, H. Morrison, and J. H. Seinfeld, 2012: Are simulated aerosol-induced effects on deep convective clouds strongly dependent on saturation adjustment? *Atmos. Chem. Phys.*, **12**, 9941–9964, doi:10.5194/acp-12-9941-2012.

Lin, Y.-L., R. D. Farley, and H. D. Orville, 1983: Bulk parameterization of the snow field in a cloud model. *J. Climate Appl. Meteor.*, **22**, 1065–1092, doi:10.1175/1520-0450(1983)022<1065:BPOTSF>2.0.CO;2.

Mansell, E. R., C. L. Ziegler, and E. C. Bruning, 2010: Simulated electrification of a small thunderstorm with two-moment bulk microphysics. *J. Atmos. Sci.*, **67**, 171–194, doi:10.1175/2009JAS2965.1.

Meyers, M. P., P. J. DeMott, and W. R. Cotton, 1992: New primary ice nucleation parameterizations in an explicit cloud model. *J. Appl. Meteor.*, **31**, 708–721, doi:10.1175/1520-0450(1992)031<0708:NPINPI>2.0.CO;2.

Milbrandt, J. A., and M. K. Yau, 2005: A multimoment bulk microphysics parameterization. Part I: Analysis of the role of the spectral shape parameter. *J. Atmos. Sci.*, **62**, 3051–3064, doi:10.1175/JAS3534.1.

Morrison, H., and J. O. Pinto, 2005: Mesoscale modeling of springtime Arctic mixed-phase stratiform clouds using a new two-moment bulk microphysics scheme. *J. Atmos. Sci.*, **62**, 3683–3704, doi:10.1175/JAS3564.1.

——, and W. W. Grabowski, 2007: Comparison of bulk and bin warm rain microphysics models using a kinematic framework. *J. Atmos. Sci.*, **64**, 2839–2861, doi:10.1175/JAS3980.

——, and ——, 2008a: Modeling supersaturation and subgrid-scale mixing with two-moment bulk warm microphysics. *J. Atmos. Sci.*, **65**, 792–812, doi:10.1175/2007JAS2374.1.

——, and ——, 2008b: A novel approach for representing ice microphysics in models: Description and tests using a kinematic framework. *J. Atmos. Sci.*, **65**, 1528–1548, doi:10.1175/2007JAS2491.1.

——, and ——, 2011: Cloud-system resolving model simulations of aerosol indirect effects on tropical deep convection and its thermodynamic environment. *Atmos. Chem. Phys.*, **11**, 10 503–10 523, doi:10.5194/acp-11-10503-2011.

——, and J. A. Milbrandt, 2015: Parameterization of cloud microphysics based on the prediction of bulk ice particle properties. Part I: Scheme description and idealized tests. *J. Atmos. Sci.*, **72**, 287–311, doi:10.1175/JAS-D-14-0065.1.

——, G. Thompson, and V. Tatarskii, 2009: Impact of cloud microphysics on the development of trailing stratiform precipitation in a simulated squall line: Comparison of one- and two-moment schemes. *Mon. Wea. Rev.*, **137**, 991–1007, doi:10.1175/2008MWR2556.1.

Phillips, V. T. J., L. J. Donner, and S. T. Garner, 2007: Nucleation processes in deep convection simulated by a cloud-resolving model with double-moment bulk microphysics. *J. Atmos. Sci.*, **64**, 738–761, doi:10.1175/JAS3869.1.

Politovich, M. K., and W. A. Cooper, 1988: Variability of supersaturation in cumulus clouds. *J. Atmos. Sci.*, **45**, 1651–1564, doi:10.1175/1520-0469(1988)045<1651:VOTSIC>2.0.CO;2.

Rutledge, S. A., and P. V. Hobbs, 1984: The mesoscale and microscale structure and organization of clouds and precipitation in midlatitude cyclones. Part XII: A diagnostic modeling study of precipitation development in narrow cloud-frontal rainbands. *J. Atmos. Sci.*, **41**, 2949–2972, doi:10.1175/1520-0469(1984)041<2949:TMAMSA>2.0.CO;2.

Shipway, B. J., and A. A. Hill, 2012: Diagnosis of systematic differences between multiple parametrizations of warm rain microphysics using a kinematic framework. *Quart. J. Roy. Meteor. Soc.*, **138**, 2196–2211, doi:10.1002/qj.1913.

Squires, P., 1952: The growth of cloud drops by condensation. 1. General characteristics. *Aust. J. Sci. Res.*, **A5**, 59–86.

Stevens, B., R. L. Walko, and W. R. Cotton, 1996: The spurious production of cloud-edge supersaturation by Eulerian models. *Mon. Wea. Rev.*, **124**, 1034–1041, doi:10.1175/1520-0493(1996)124<1034:TSPOCE>2.0.CO;2.

Szumowski, M. J., W. W. Grabowski, and H. T. Ochs III, 1998: Simple two-dimensional kinematic framework designed to test warm rain microphysical models. *Atmos. Res.*, **45**, 299–326, doi:10.1016/S0169-8095(97)00082-3.

Thompson, G., R. M. Rasmussen, and K. Manning, 2004: Explicit forecasts of winter precipitation using an improved bulk microphysics scheme. Part I: Description and sensitivity analysis. *Mon. Wea. Rev.*, **132**, 519–542, doi:10.1175/1520-0493(2004)132<0519:EFOWPU>2.0.CO;2.

Xue, H., and G. Feingold, 2006: Large-eddy simulations of trade wind cumuli: Investigation of aerosol indirect effects. *J. Atmos. Sci.*, **63**, 1605–1622, doi:10.1175/JAS3706.1.